Leaf oscillation and upward ejection of droplets in response to drop impact

Tristan Gilet [*,†]
Microfluidics Lab, Department of Aerospace and Mechanical Engineering, University of Liège, 4000 Liège, Belgium

Loïc Tadrist
Institut des Sciences du Mouvement, Aix-Marseille Université, 13100 Aix-En-Provence, France

(Received 25 December 2024; accepted 18 March 2025; published 2 May 2025)

Plant leaves vibrate in response to raindrop impacts. When the resulting inertial forces are sufficient, residual rainwater at the leaf surface may be dislodged and ejected in the form of droplets. These droplets participate to the transport of pathogenic spores, including in the upward direction. The present experimental work aims at exploring the limits of this mechanism, in the simpler case of a single drop impacting an initially dry artificial leaf. The transfer of momentum from the impacting drop to the leaf is rationalized. The conditions of droplet ejection are identified, and these droplets are shown to inherit from the velocity of the leaf. Finally, these results are extrapolated to estimate the frequency of upward transport events as a function of rainfall intensity for a distribution of raindrop sizes.

DOI: 10.1103/PhysRevFluids.10.053601

I. INTRODUCTION: RAIN-INDUCED FOLIAR PATHOGEN DISPERSAL

Rainfalls play a major role in the propagation of many pathogenic fungi responsible for foliar diseases [1]. The rain-induced epidemic dispersal of spores has been quantified for several fungi on the leaves of major crops, for example, *Septoria glycines* on soybean [2], *Zymoseptoria tritici* on wheat [3], *Fusarium culmorum* and *Fusarium poae* on wheat, maize and rice [4], *Fusarium graminearum* on wheat [5], and *Pyrenopeziza brassicae* on winter oilseed rape [6]. The damages caused by these fungi are severe. For example, *Zymoseptoria tritici* generates around 20% of yield loss for fungicide-free wheat (reduced to 10% with fungicide application) [7]. Understanding the mechanisms of spore dispersal is key to optimize both timing and amount of fungicides, as well as to the design of cultivar mixtures that minimize this dispersal [8].

Dispersal measurements. The dispersal potential was mostly quantified by placing a point source of spores and by positioning collectors at a distance from this source. The spores were initially either on a real leaf [9,10], on a fruit [11,12], on some ground cover [13,14], or on an artificial support that was sometimes inclined [9] (e.g., a shallow reservoir of spore-laden water [8,15], or cloth [16]). The dispersal was then operated through either (i) some real rainfall in field experiments, or (ii) through simulated rainfall, or (iii) through individual raindrop impacts in laboratory experiments [17]. Obviously, the latter provided more controllable dispersal conditions and allowed to investigate the influence of raindrop parameters on dispersal. The distribution of ejected droplet properties (number, diameter, position) was estimated from the droplets that reached the collectors [18]. Moreover, after incubation, the distribution of both spores and subsequent lesions in leaf tissues was

*Contact author: tristan.gilet@uliege.be
†www.microfluidics.uliege.be

also retrieved [19]. Dispersal seems to be marginally sensitive to spore shape [4,18]. Some fungi, for example *Zymoseptoria tritici*, release two kinds of spores that are, respectively, wind-dispersed and rain-dispersed. The wind-dispersed spores, named ascospores, result from the sexual reproduction of the fungus on infected crop debris, and they are dispersed horizontally, early in the season [20]. The rain-dispersed spores, named pycnidiospores, result from asexual reproduction and they are released later, when the new crop is growing [21]. Pycnidiospores are responsible for the epidemic stage of the disease. Their horizontal dispersal is of relative interest, because the wind-driven dispersal of ascospores has already distributed the fungus across the field [22]. Nevertheless, horizontal dispersal of pycnidiospores may be key to the propagation of specific pathogen genotypes [23]. By contrast, the vertical rain-induced dispersal of pycnidiospores, between leaves positioned at different heights of the same plant, is crucial as it allows younger leaves to be infected by older ones during the epidemic stage [20,21].

Empirical laws. The number N of either droplets or spores collected after rain-induced dispersal decreases approximately as $N = ae^{-X/b}$, where X is the distance from a point source of inoculum, either in horizontal or vertical direction [4]. The factor a increases with the Weber number $\mathrm{We} = \rho DV^2/\sigma$ of the impacting raindrop [10,24], where ρ is the water density, σ is the water surface tension, D is the raindrop diameter and V is the raindrop speed at impact. The characteristic distance of decay b decreases with increasing compliance of the substrate [25]: it is shorter for either lighter and more flexible leaves and ground cover (e.g., straw, clover) [2,3,26], or deeper liquid films/pools [15]. This distance b is also strongly dependent on the dispersal event: it may go from 2 cm for single raindrop impacts [17] to 25 m for the multiple successive impacts of an artificial rainfall [26]. The maximum height h at which a single splashing raindrop may shoot spore-laden droplets has been shown in agreement with the empirical law $h = h_0 \log(DV/c_0)$ where the parameters $h_0 \sim 25$ cm and $c_0 \sim 80\,\mathrm{cm}^2/\mathrm{s}$ depend on the splashed surface [13,27].

Spore contents. By opposition to wind dispersal in which each spore lands at a different place, dispersal through raindrop splash conveys all the spores loaded in a given splash droplet to the same location as that droplet. For droplets emitted from a [0.5, 1]-mm-thick spore suspension, the number of spores per droplet is proportional to the square of the droplet diameter [18]. A similar increase of the number of spores with droplet diameter was observed for splash on fruits [12,28]. Consequently, a majority of spores is carried by droplets with a diameter larger than 200 μm [29]. These droplets are mostly in a ballistic regime for which the trajectory can be determined from gravity and drag forces, without significant influence of turbulence [30].

Dispersal models. Several theoretical frameworks were proposed to model the rain-induced dispersal of spores. The simplest frameworks represented dispersal with a horizontal diffusion equation [11,31], for which the diffusion coefficient had to be adjusted by almost an order of magnitude depending on the plant or substrate [11]. In Monte Carlo models, dispersal was often simply represented by a probability for spores to transition from one position to another within the canopy [6,32,33]. In more advanced Monte Carlo simulations, droplets were generated according to prescribed distributions of diameter and initial velocity, and their trajectory was calculated [34,35], including their potential interception by another leaf [36,37].

Limitations. Neither the aforementioned laboratory experiments nor the models and numerical simulations of dispersal considered an informed and accurate representation of the drop splash on plant leaves and subsequent droplet ejections. Assuming that raindrops indeed splash on spore-laden thin liquid films, the droplet ejection pattern is expected to strongly depend on the film thickness [38]. Moreover, there is no evidence that rainwater preferably forms films or puddles on sporulating leaves. Impacts next to sessile drops generate a very different ejection pattern that is more efficient at shooting droplets in a given direction [25,39]. Other mechanisms were also proposed to explain spore dispersal, including dry spores being pushed away by the impact and spreading of the raindrop [40,41], spores captured in bouncing droplets [42,43], spore-laden droplets jumping upon coalescence of condensation-formed sessile droplets on superhydrophobic leaves [44,45], or spores splashed from puddles in splash cups [43].

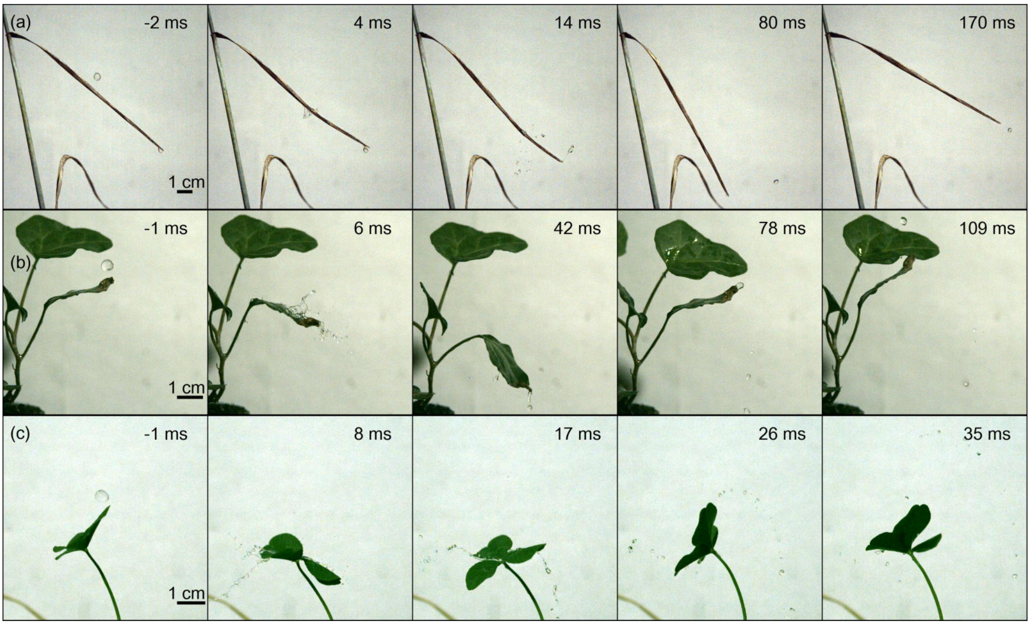

FIG. 1. Snapshots from three different recordings showing impacts of single water drops of diameter $D = 4.76\,\text{mm}$ on three different plant leaves. (a) Impact at speed $V = 4.8\,\text{m/s}$ on a necrotized wheat leaf. (b) Impact at $V = 5.2\,\text{m/s}$ on an ivy leaf. (c) Impact at $V = 5.2\,\text{m/s}$ on a clover leaf. The scale bars are 1 cm in each set of snapshots. In panel (a), the blade length is $L = 119\,\text{mm}$ and the natural frequency of the first bending mode is $\omega = 25\,\text{rad/s}$. In (b), the blade length is $L = 20\,\text{mm}$ and the natural frequency of the first bending mode is $\omega = 37\,\text{rad/s}$. In panel (c), the blade length is $L = 16\,\text{mm}$ and the natural frequency of the first bending mode is $\omega = 131\,\text{rad/s}$. The time from impact at which each snapshot was taken is indicated in the upper-right corner. The corresponding movies are available in the Supplemental Material [46].

Preliminary visualizations. To initiate this work, impacts of water drops (diameter $D = 4.76\,\text{mm}$, impact speed $V \sim 5\,\text{m/s}$) on several plant leaves were observed with high-speed imaging. Figure 1 illustrates three of such impacts on three leaves from different living plants. The first was a necrotized wheat leaf (i.e., its tissues were already dry and consequently stiffer than those of a fresh and healthy leaf). The second and third leaves were from ivy and clover, respectively. Some water from a previous impact was already present at the tip of the wheat leaf [Fig. 1(a)]. Upon impact, each leaf bent downward. At the same time, the drop spread beyond the leaf edges and formed a liquid sheet (Fig. 1, second column) that quickly fragmented into ligaments and droplets [47]. Owing to the inclination of the leaf blade, these droplets were mostly ejected downwards (Fig. 1, third column) [48]. Not all the water from the drop was ejected, and the residue accumulated at the leaf tip [Fig. 1(a) at 80 ms, Fig. 1(b) at 42 ms, Fig. 1(c) at 8 ms]. Then the leaf sprang back upwards, and the water residue was stretched beyond the leaf tip thanks to the inertial forces associated to the leaf motion. The residue then broke up into one or several droplets that were mostly ejected upwards (Fig. 1, last column). The clover leaf (the smallest of the three considered leaves) shooted droplets at up to 2 m/s of upward vertical velocity. Such droplets would ballistically reach a height of almost 20 cm above the leaf.

This impact scenario is able to generate upward droplet ejections at distances compatible with the observations of vertical rain-induced spore dispersal. Moreover, it has been observed for a variety of plant leaves. The water of these ejected droplets may originate either from the impacting raindrop [Figs. 1(b) and 1(c)], or from some water residue already present on the leaf [Fig. 1(a)] [25]. This residue would be able to dissolve the mucilage that usually surrounds spores [1], and would thereby contain the spores in suspension at the time of its ejection from the leaf [49]. Consequently, the scenario reported here is likely to significantly contribute to the vertical dispersal of pathogenic spores in crops.

Goals and structure. The present paper aims at rationalizing the scenario in which a raindrop impacts a dry plant leaf, the leaf bends and vibrates, and droplets (originating from the raindrop) are ejected thanks to the inertial forces associated to the leaf motion. This scenario can be seen as a simplification of the more complex and realistic scenario in which the raindrop impacts a leaf already loaded with residual water from previous impacts. In Sec. II, a short literature review of drop impacts on compliant surfaces is provided. The experimental setup, the explored configurations and the data processing are described in Sec. III. Section IV presents the phenomenology associated to the considered drop impacts. Section V presents and discusses experimental results on momentum transfer from the impacting drop to the leaf and on subsequent droplet ejections. Finally, an extrapolation of the results to a complete rainfall is provided in Sec. VI.

II. STATE-OF-THE-ART: RELATED STUDIES ON DROP IMPACTS AND DROPLET EJECTIONS

Timescales. Several works have already investigated drop impacts on various compliant surfaces, including cantilever structures [50–53], soft substrates [54–56] and membranes [57,58]. Three characteristic times may be identified as relevant for such impacts: (1) the impact time $t_\mathrm{i} = D/V$ needed by the drop to crush on the substrate, (2) the capillary time $t_\sigma = \sqrt{\rho D^3/(6\sigma)}$ required by capillary forces to match with inertial forces at drop scale (this time corresponds to both the contact time of bouncing drops at low impact speed and the characteristic time of fragmentation during splash at high impact speed), and (3) the characteristic period $(2\pi/\omega)$ associated to the vibration of the compliant surface at natural angular frequency ω. The ratio $t_\sigma/t_\mathrm{i} = \sqrt{\mathrm{We}/6}$ is a function of the Weber number.

In the regime $t_\mathrm{i} \lesssim t_\sigma$, drops usually rebound on superhydrophobic surfaces and stick to other surfaces. For compliant surfaces with $(2\pi/\omega) \sim t_\sigma$, the rebound is more efficient, with shorter contact time and reduced maximal spreading [51–53,55,56,58–60]. By contrast, the post-spreading recoil of drops impacting on nonsuperhydrophobic compliant surfaces with $(2\pi/\omega) \sim t_\sigma$ was less than on rigid surfaces [61,62]. In the regime $t_\mathrm{i} \ll t_\sigma$ (i.e., We $\gg 100$) in which droplets are likely to splash, the splash can be diminished and even suppressed on compliant substrates for which $(2\pi/\omega) \sim t_\mathrm{i}$ [54,57]. Finally, in the case of extreme substrate compliance and for We ~ 1, capillary forces may be sufficient to induce the wrapping of the substrate around the impacting drop [63].

Plant leaves. Drop impacts on real plant leaves (either clamped at the petiole basis—simple leaf, or emerging from the shoot—sessile leaf) have already been investigated in, e.g., Refs. [25,49,64–67]. The leaf motion induced by the impact can be decomposed into several vibration modes. The relative amplitude at which each of these modes is excited depends on the impact point position [65,68]. The modes are shaped by the structural properties of the leaf, and they may involve a subtle combination of petiole bending and twisting, as well as bending of the leaf blade in both longitudinal and transversal directions [65,69,70]. The mode of lowest frequency ω usually corresponds to the longitudinal bending of the petiole (and possibly the blade). For the leaves considered in the aforementioned studies, raindrop impacts were mostly in the regime $t_\sigma \ll (2\pi/\omega)$, for which drop spreading and possible fragmentation are completed before the leaf reaches its most downward position.

Liquid sheet. Impacting raindrops may spread beyond the edges of plant leaves [47], especially when the leaf blade is narrow. In such a case, illustrated in Fig. 1, the liquid beyond the edge forms a sheet that first expands then collapses, emitting droplets at both steps. An analog phenomenon is observed for high Weber impacts on superhydrophobic surfaces, as water spreads without significantly wetting them [71]. This mechanism was investigated extensively in the axisymmetric case of a drop impacting at the center of a pole [72–79]. Alternative geometries included straight [47,48] and polygonal edges such as in toothed leaves [80,81]. When the impact position is too close to the leaf edge, the drop momentum is not entirely transferred to the leaf, and the liquid sheet develops in a plane inclined with respect to the blade [47,82]. This necessarily happens when raindrops impact fiber-shaped leaves such as pine needles [83–87].

Ejections induced by substrate motion. As seen in Fig. 1, the inertial forces resulting from the substrate motion may also displace water residues on its surface, and possibly expel them in the form of droplets. This phenomenon was studied in the context of the shaking of wet mammals [88], then in the more ideal case of a sessile drop on a vertically vibrated hydrophobic cantilever beam [89]. Two main modes of droplet ejection were identified: (1) the sessile drop slides to the tip of the leaf in response to the centrifugal force, then forms a ligament beyond the tip that fragments in droplets, and (2) the sessile drop elongates in the direction normal to the leaf in response to the Euler force, then either takes off or pinches off. In Ref. [89], the frequency range in which the beam was vibrated corresponded to $(2\pi/\omega) \sim t_\sigma$, namely, a range in which the sessile drop vibrated in resonance with the beam. On plants, sessile water residues can hardly be excited by the fundamental vibration mode of leaves since $t_\sigma \ll (2\pi/\omega)$ for this mode.

III. MATERIALS AND METHODS

A list of the main variables and parameters defined in this study is provided in Table I.

TABLE I. Variables used in this work, and corresponding range of values in the present experiments.

Variable	Definition	Range
t	Time	–
ϕ	Phase of oscillation	$[0, 2\pi]$ rad
x, y, z	Coordinates	–
x_i	Impact position	–
r	Distance to rotation axis	–
$\theta(t)$	Blade inclination	–
D	Drop diameter	[2.26, 4.76] mm
M	Drop mass	[5.6, 57.9] mg
V	Drop impact velocity	[1.1, 5.3] m/s
ρ	Water density	1 mg/mm^3
σ	Water surface tension	0.072 N/m
We	Weber number	[85, 1926]
R_s	Maximum spreading radius	[5.1, 12.5] mm
L	Leaf length, from rotation axis	[21.4, 66.4] mm
α	Half-angle at blade tip	[15, 90]$^\mathrm{o}$
I	Leaf moment of inertia	[16, 791] g.mm^2
ω	Fundamental leaf frequency	[24, 231] rad/s
β	Decay rate	[0.8, 6.6] rad/s
ρ_a	Air density	1.2×10^{-3} mg/mm^3
$\dot{\theta}_0$	Initial angular velocity	[1.3, 158] rad/s
v_L	Maximum velocity of leaf tip	[0.4, 3.4] m/s
v_LM	Theoretical maximum speed of leaf tip	[0.5, 3.3] m/s
a_c	Centrifugal acceleration	[0.1, 537] m/s^2
a_E	Euler acceleration	[1.9, 723] m/s^2
g	Acceleration of gravity	9.81 m/s
$\mathrm{Bo_c}$	Bond number based on a_c	$[7 \times 10^{-3}, 43]$
Bo_c^*	Bond number at ejection threshold	2.4
d	Diameter of ejected droplets	[0.09, 4.1] mm
v_x, v_y	Droplet velocity components at the time of ejection	[−2.6, 2.8] m/s
h	Height reached by ejected droplets	[0, 413] mm

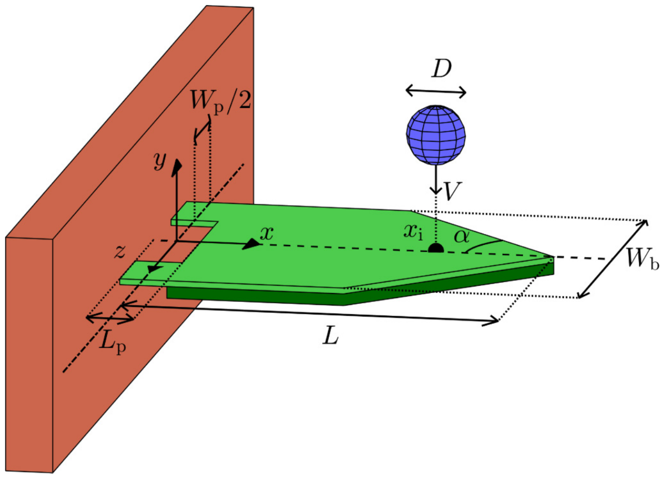

FIG. 2. Schematic sketch of a drop (blue) impacting an artificial leaf (green) clamped at its basis (brown). The blade is thickened (dark + light green) while the petiole is not (light green only). The x axis corresponds to the symmetry axis of the leaf when horizontal (dashed line). The leaf rotates about the dash-dotted line which coincides with the z axis. The y axis is vertical, pointing upwards, and perpendicular to x and z. Most relevant leaf and drop dimensions are indicated in the sketch and described in the main text.

A. General description of the setup

In each experiment, an artificial leaf was clamped in a horizontal position (Fig. 2). The leaf was mainly articulated through the bending of its petiole. It was mechanically designed to prevent any significant twisting of the petiole or bending of the blade. A water drop was released from a dripping point vertically above the leaf. The drop impacted the leaf blade and induced an oscillatory rotation of the blade around a horizontal axis close to the petiole. This motion in turn forced the water residue on the leaf to move and break up in droplets ejected from the leaf. The observed leaf vibration was always largely underdamped.

Absolute coordinates (x, y, z) are defined, with an origin at the intersection of the main rotation axis of the leaf blade and its plane of symmetry. The x axis is horizontal and the y axis is vertical. Both are included in the plane of symmetry of the blade, $x > 0$ at the leaf tip, and $y > 0$ above the rotation axis of the blade. The z axis is horizontal and perpendicular to the aforementioned plane of symmetry; it approximately corresponds to the rotation axis of the leaf blade.

The impact was filmed simultaneously from the side with a monochrome high-speed camera (FastCam Mini UX-100, Photron—with Nikon lens 24–85 mm) and from the top with a color high-speed camera (Phantom MIRO M110, Vision Research, with Nikon lens 60 mm). Both views were filmed at 1000 frames per second. In the side view, the optical axis of the camera was aligned with the z axis and a homemade LED light was placed on the other side of the leaf (back lighting). In the top view, the optical axis of the camera was in (x, y) plane and inclined either at 45° or 71° from the horizontal, depending on the experiment. A home-made LED light was placed next to the camera (front lighting). Most quantitative data are obtained by processing side-view movies. The top view completes the qualitative description of the phenomena. A picture of the experimental setup is available in the Supplemental Material [46].

B. Artificial leaves

Manufacturing. Twenty-four artificial leaves were fabricated by cutting 2D shapes in polyimide sheets (DuPont Kapton HN) of thickness $H_p = 75\,\mu\text{m}$ and area density $\rho_{Ap} = 0.11\,\text{mg/mm}^2$. The measured advancing and receding contact angles of water on polyimide were $\theta_a = 80^\circ(\pm 1^\circ)$ and

$\theta_r = 31^\circ(\pm 1^\circ)$. Each leaf comprised a petiole and an adjacent blade in a cantilever design (Fig. 2). The leaves were symmetrical with respect to the (x, y) plane. When the leaf is horizontal, its dimensions along x are referred as lengths, its dimensions along z are referred as widths, and its dimensions along y are referred as thicknesses. The blade was stiffened by sticking an identical shape cut in tape (thickness 325 μm, area density $0.34\,\mathrm{mg/mm^2}$) on the underside of the polyimide sheet, so the total thickness of the blade was $H_b \simeq 400$ μm and the corresponding area density was $\rho_{Ab} \simeq 0.45\,\mathrm{mg/mm^2}$. By contrast, the petiole was only made of the polyimide sheet. It consisted in either one or two rectangles, of length $L_p \simeq 3$ mm and total width $W_p \in \{8, 14, 30\}$ mm. The blade consisted in a rectangle of width $W_b = 30$ mm and an adjacent triangular tip of half-angle $\alpha \in \{15, 30, 45, 60, 90\}^\circ$. This tip was set up to allow the observation of any drip-tip-related ejection mechanism [90]. The total length of the blade (rectangle and triangle) was $L_b \in \{20, 35, 50, 65\}$ mm. The mass of each leaf, measured with an analytical scale (Pioneer PX224M, accuracy < 1 mg), ranged in $[167, 697]$ mg, and it was within 4% of the mass calculated from the dimensions and area density of the leaf parts (polyimide and tape). Plant leaves on which vibrations upon raindrop impacts were investigated are in the same range of length and mass [25,64–67,91].

Mechanical behavior. The petiole was firmly clamped on its side opposite to the blade. The inclination of the clamp was adjusted as a function of the leaf weight, to ensure that the blade was horizontal when at rest [92]. The bending stiffness k of the petiole is defined as the ratio between the bending moment applied to the petiole, and the corresponding angular deflection θ of the blade basis with respect to the clamp. According to the elastic beam theory, this bending stiffness is

$$k = \frac{E H_p^3 W_p}{12 L_p}, \tag{1}$$

where $E = 2.5$ GPa is the Young's modulus of polyimide. Assuming that the tape is of similar Young's modulus, the bending stiffness of the blade is approximately $k(H_b^3 W_b L_p)/(H_p^3 W_p L_b)$. For the considered leaves, the blade was always more than six times stiffer in bending than the petiole, so in first approximation it was considered as rigid. This was confirmed from the side-view videos in which the blade was never observed to bend significantly. The artificial leaves considered in this study are representative of leaves for which the blade is rigidified by either midrib and veins or by a nonzero Gauss curvature [93].

The torsional stiffness of their petiole is of the order of $k(W_b/L_p)^2$, which is two orders of magnitude larger than k. While such high torsional stiffness is not representative of most leaves for which bending and torsional stiffnesses are of the same order of magnitude [94], it is intended in this study for the sake of kinematic simplicity. As only the petiole bent, the leaf blade mostly experienced a rigid rotation around an axis which is approximately at $L_p/2$ from the clamp (Fig. 2). This rotation axis is defined as the z axis, corresponding to $x = y = 0$. The leaf length $L = L_b + L_p/2$ is defined as the distance from the rotation axis to the leaf tip.

For some impact positions, a second vibration mode of the blade was observed during the first 50 ms, in superposition to the main mode. In this second mode, the blade rotated around an axis closer to its center of mass, with an amplitude (respectively, frequency and decay rate) at least an order of magnitude smaller (respectively, larger) than that of the main vibration mode. Higher-order modes involving elastic waves in the petiole were never observed, most likely because all the considered petioles were much shorter and lighter than the blades. Only the main vibration mode induced significant leaf acceleration, leading to fluid movements and droplet ejections reported hereafter. Therefore, in the remainder of this paper, the motion of the leaf blade is assumed to be equivalent to the solid body motion of a plate around a torsion hinge (the petiole), and it is entirely described through the time evolution of the blade inclination $\theta(t)$.

Mechanical model. Assuming that the leaf vibrates without any excitation or added load, the corresponding Newton's law of motion is that of a harmonic oscillator,

$$I\ddot{\theta} + 2\beta I\dot{\theta} + k\theta = 0, \tag{2}$$

where I is the moment of inertia of the leaf with respect to its rotation axis z, and β is the decay rate corresponding to the damping of the vibration. The blade inertia I_b is estimated as

$$I_b \simeq \rho_{Ab} \int_{L_p/2}^{L} r^2 W(r) dr, \tag{3}$$

where $W(r)$ is the local blade width at a distance r from the rotation axis. The inertia I_a associated to the added mass of air entrained by the leaf vibration is estimated from a formula valid for the 2D potential flow adjacent to a rectangular plate in rotation around one of its edges [95],

$$I_a \simeq \frac{9\pi \rho_a}{128} \int_{-W_b/2}^{W_b/2} \ell^4(z) dz, \tag{4}$$

where $\rho_a \simeq 1.2 \times 10^{-3}$ mg/mm^3 is the air density and $\ell(z)$ is the local leaf length at abscissa z (from the symmetry axis). Although this estimation of added mass is crude, it represents at most 8% of the total inertia $I = I_b + I_a$.

The solution to Eq. (2) is

$$\theta(t) = \frac{\dot{\theta}_0}{\omega} e^{-\beta t} \sin(\omega t), \tag{5}$$

where $\dot{\theta}_0$ is the initial angular velocity and ω is the frequency of leaf vibrations. This frequency can be approximated by the natural frequency

$$\omega \simeq \sqrt{\frac{k}{I}}, \tag{6}$$

provided that $\beta \ll \omega$. Under the same assumption, the velocity of the leaf tip is approximately

$$L\dot{\theta} \simeq v_L e^{-\beta t} \cos(\omega t), \tag{7}$$

with $v_L = L\dot{\theta}_0$.

The vibration frequency ω and decay rate β were measured for each leaf, first by impacting a metal bead instead of a drop. The description and results of this complementary experiment with beads on leaves are reported in Appendix A 1. Parameters ω and β were also measured for each drop impact. As seen in this Appendix, the added mass of liquid residues results in a slight decrease of ω. Moreover, the additional viscous damping in these residues results in an increase of β [96]. Nevertheless, for all leaves, leaf vibrations were always largely underdamped ($\beta \lesssim 0.1\omega$) so the approximation of Eq. (6) is valid.

In first approximation, a liquid residue at the surface of a leaf, at a distance r from the rotation axis, experiences a centrifugal acceleration of

$$a_c = r\dot{\theta}^2 \tag{8}$$

pointing outward along the blade. It also experiences a Euler acceleration of

$$a_E = r\ddot{\theta} \tag{9}$$

in the direction normal to the blade, counted positive downward. Gravity components $g \sin\theta$ and $g \cos\theta$ complement the centrifugal and Euler accelerations, respectively.

The main geometrical and mechanical properties of the 24 leaves are summarized in Table II. The ranges of leaf length, inertia and frequency overlap with those of previous studies on drop-induced leaf vibrations [65,66]. The petiole length L_p could not be precisely measured, and its exact value was strongly influenced by the fine positioning of the artificial leaf in the clamp. The values reported in Table II correspond to an adjustment of L_p for each leaf, in the range [2, 4] mm, to ensure a match between the measured ω for beads on leaves and the prediction of Eq. (6).

TABLE II. Main leaf parameters (defined in the main text and in Fig. 2). A number and a color are associated to each leaf. Geometry parameters L_b, α, and W_p are obtained by geometrical design. The leaf frequency ω was measured with bead impacts. Parameters L_p and I are calculated through Eqs. (1), (3), (4), and (6).

Leaf No.	Color	L_b [mm]	α [deg]	W_p [mm]	L_p [mm]	I [g mm^2]	ω [rad/s]
L1		65	15	14	2.2	416	37
L2		35	30	14	2.3	77	86
L3		35	30	30	3.0	80	106
L4		65	30	14	2.7	791	24
L5		20	45	14	2.8	16	165
L6		50	45	14	2.3	413	37
L7		20	60	14	2.7	24	139
L8		35	60	30	2.7	158	79
L9		35	60	8	2.2	154	47
L10		20	90	14	2.8	45	98
L11		35	90	30	2.8	229	64
L12		50	90	14	2.5	656	27
L13		20	45	30	3	16	231
L14		20	60	30	2.9	25	195
L15		20	60	8	2.9	25	99
L16		35	30	8	2.6	78	29
L17		50	30	14	2.6	301	40
L18		50	30	8	2.5	300	31
L19		50	45	8	2.6	417	25
L20		50	60	30	2.7	508	45
L21		50	60	8	2.6	506	24
L22		65	15	30	2.5	420	50
L23		65	30	30	2.8	793	34
L24		35	30	14	3.4	81	65

C. Impacting drops

The dripping point was smoothly supplied with DI water thanks to a syringe pump (AL-300, World Precision Instruments). The flow rate was adjusted to keep the dripping period between 5 and 20 s. In such conditions, it was possible to stop the pump shortly after each impact, to avoid a second impact in the recordings. The flow rate was sufficiently low to allow regular dripping [97].

The drop diameter D was measured by image processing on high-speed videos for each impact. Median diameter values of 2.26 mm, 3.46 mm, or 4.76 mm were achieved by taking three different drip tips (a blunt 27G needle, a blunt 18G needle, and a male Luer-Lock, respectively). These diameters correspond to the upper range of raindrops (i.e., mostly observed during heavy rainfalls) and to drips from overhanging vegetation [98]. There are two reasons to focus on this upper range: (1) field measurements suggest that heavy rainfalls are more effective at dispersing spores upward than light rainfalls [21], and (2) small raindrops cannot generate leaf vibrations of sufficient amplitude to induce droplet ejections. The interquartile of the distribution of measured D was less than 36 µm for every drip tip. Five heights of the dripping point (with respect to the leaf) from 7 cm to 1.7 m were considered, thereby varying the impact speed V of the drop on the leaf between 1.1 m/s and 5.3 m/s. This impact speed was also measured by image processing for each impact. Such impact speed is significantly lower (15%–70%) than the terminal velocity of raindrops, but it matches well with the velocity range of drips [99]. Nine different drop types defined by (D, V) were tested (out of 3×5), as summarized in Table III. For each drop type, the interquartile of the corresponding distribution of measured V was always less than 0.06 m/s. The

TABLE III. Main parameters of each drop type (defined in the main text). A number and a symbol are associated to each drop type. Parameters D and V were measured, and their median value is reported. The Weber number We is calculated from these measurements. The maximum spreading radius R_s was measured in independent experiments of impacts on a rigidified polyimide substrate.

Drop No.	Symbol	D [mm]	V [m/s]	We [−]	R_s [mm]
D1	►	4.76	3.0	614	10.0
D2	◄	4.76	4.1	1148	11.5
D3	▲	4.76	5.3	1926	12.5
D4	▼	3.46	3.0	449	7.2
D5	•	3.46	4.1	835	7.9
D6	■	3.46	5.1	1315	9.0
D7	♦	2.26	4.8	749	5.1
D8	★	4.76	1.1	85	6.4
D9	★	4.76	1.9	253	9.0

Weber number We $= \rho D V^2/\sigma$, calculated from the median values of D and V, goes from We $= 85$ for configuration D8 to We $= 1926$ for configuration D3.

The impact point on the leaf was varied by slightly translating either the leaf clamp or the dripping point. Intrinsic variations of the impact point induced by the random motion of the falling drop [100] were observed, mostly at the largest release heights. To make sure that the twist mode was not significantly excited, only experiments in which the impact point was at less than 2 mm from the symmetry axis ($z = 0$) were recorded and analyzed.

The maximum spreading radius R_s experienced by these drops when they impacted a rigid substrate [101] was measured in separate experiments and is reported in Table II. The leaf width $W_b = 30$ mm was set to satisfy $R_s < W_b/2$ for all drop impacts, thereby avoiding any spreading (and subsequent ejections) beyond the side edges of the leaves.

D. Impact configurations

An impact configuration is defined as a combination of a drop type with a given leaf. In total, 70 configurations were explored (out of 24×9). They were selected to span a large range of leaf motion amplitude. About half of them led to droplet ejections induced by leaf motion. The considered configurations, as well as the number of impacts recorded in each, are reported in Fig. 3. In one configuration (L24, D2), 75 impacts were recorded, with a corresponding impact point distributed over the whole length of the leaf. Other configurations comprised between 2 and 13 impacts at different positions, with more impacts recorded when the outcome (potential droplet ejections) was visibly more sensitive to the impact position. In total, 424 drop impacts on artificial leaves were recorded and processed. Between successive impacts, residual water on the leaf was gently wiped with a tissue compatible with clean-room work. Care was taken to avoid contaminating the leaf surface and potentially modifying its wettability. No drift of the range of contact angles or abnormal wetting behavior was witnessed in the side-view videos.

E. Data processing

The initially falling drop, the leaf blade and the droplets ejected through leaf oscillations (i.e., every droplet except those ejected from the liquid sheet formed right after impact) were tracked with conventional image processing techniques applied to the side view movies. Prior to this tracking, the position of these droplets at the time of their ejection t_e was encoded manually to guarantee an accurate tracking with a success rate of 100%. The position (x, y) of both falling drop and ejected droplets, their diameter, and the inclination θ of the blade were recorded at each time t. Any slight

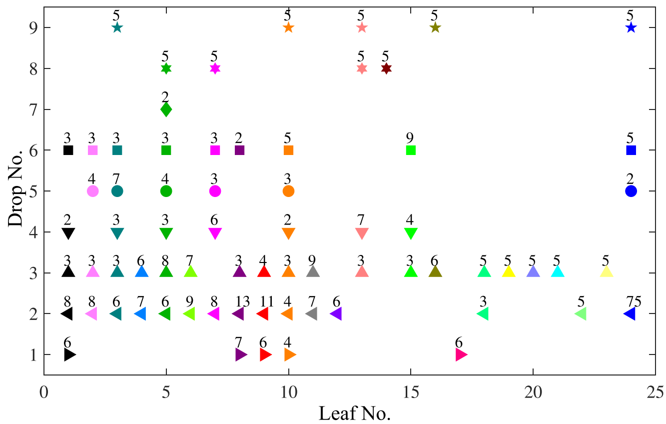

FIG. 3. Seventy impact configurations, each associating a leaf (color) and a drop (symbol) were considered in this work. The number of recorded drop impacts (at different positions) is indicated with a number right above the data point corresponding to each configuration.

twist or bend of the blade results in an error on θ. This error was estimated from variations of eccentricity of an ellipse fitted on the blade detected in the side view. The impact speed V and the impact position x_i (from the rotation axis) were calculated from the trajectory of the falling drop. The angular frequency ω and the decay rate β were calculated by fitting Eq. (5) on several oscillation periods of the measured $\theta(t)$. The phase is defined as the time normalized by the leaf oscillation period, $\phi = \omega t/(2\pi)$. Then the initial angular velocity $\dot{\theta}_0$ was determined by fitting Eq. (5) on the first third of oscillation period (i.e., $\phi \in [0, 1/3]$). The relative error on $\dot{\theta}_0$ results from both the aforementioned error on $\theta(t)$ and an estimated error of $\pm1.2\%$ on ω resulting from the fitting process. Slight variations of frequency and angular momentum induced by significant droplet ejections were detectable, but later neglected. The diameter d of each ejected droplet was calculated by averaging diameter measurements at successive times. The velocity components (v_x, v_y) of each droplet at the time of ejection were obtained by fitting the laws of free fall: $x(t) = x_0 + v_x(t - t_\mathrm{e})$ and $y(t) = y_0 + v_y(t - t_\mathrm{e}) - g(t - t_\mathrm{e})^2/2$.

IV. PHENOMENOLOGY

Description of an impact. An example of remarkably efficient droplet ejection is shown in Fig. 4. It corresponds to the drop of largest momentum, D3, impacting the lightest leaf, L5, at a distance $L - x_\mathrm{i} = 8.6$ mm from the leaf tip (Fig. 4, $\phi \lesssim 0$). The drop transfers a large part of its momentum to the leaf blade that rotates downwards (Fig. 4, $\phi = 0.15$). In the meantime, the drop spreads on the blade, crosses its edge, and subsequently generates a liquid sheet surrounded by a rim from which droplets are ejected [47]. By contrast to impacts on a rigid surface [47], the sheet is curved in three dimensions, owing to the leaf motion concomitant to the sheet formation (Fig. 4, $\phi = 0.15$). The sheet quickly disintegrates into droplets that are mostly ejected downward, in response to both inclination and velocity of the blade at the time of sheet formation (Fig. 4, $\phi = 0.40$) [48].

We define a stroke as the movement made by the leaf over half of its oscillation period. According to this definition, the stroke number is given by $\lceil 2\phi \rceil$ and the first stroke corresponds to $0 < \phi < 0.5$. The formation and breakup of the liquid sheet occur during this first stroke. During the second stroke, the leaf moves upward, and the remaining water on the blade is expelled from the leaf in response to inertial forces. It forms a long fluid ligament attached to the leaf tip (Fig. 4, $\phi = 0.90$) [102]. As the leaf tip now accelerates downward, the ligament is stretched and it breaks up into a string of droplets (Fig. 4, $\phi = 1.00$) [102].

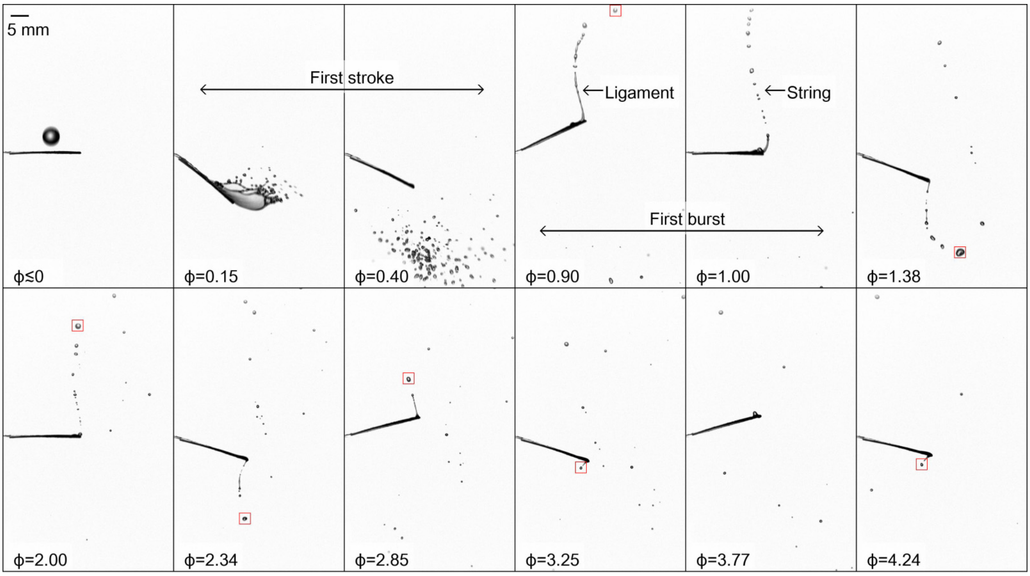

FIG. 4. Seven successive ejection bursts observed upon impact of a drop D3 at $L - x_\mathrm{i} = 8.6$ mm from the tip of leaf L5 (period 38 ms). A red box is drawn around first-in-a-burst droplets. The phase ϕ at which each snapshot was taken is indicated in the lower left corner. The scale bar is 5 mm. The corresponding movie is available in the Supplemental Material [46].

We define a burst as the formation and breakup of a ligament in response to a leaf stroke. The first burst thus takes place in the fourth and fifth snapshots, during the second stroke. It is quickly followed by another burst during the third stroke, in which another ligament is formed and broken up (Fig. 4, $\phi = 1.38$). As the leaf keeps oscillating, four successive bursts are observed, once per stroke until the seventh stroke (Fig. 4, $2.00 \leqslant \phi \leqslant 3.25$).

The leaf oscillations are progressively damped and the liquid residue on the leaf blade gets depleted. Consequently, the successive ligaments are of decreasing size. They are also ejected more and more radially inward (i.e., inside the circular arc described by the leaf tip), which is a consequence of the centrifugal acceleration decreasing faster than the Euler acceleration ($a_\mathrm{c} \sim e^{-2\beta t}$ while $a_\mathrm{E} \sim e^{-\beta t}$). The eighth stroke is the first one where a ligament is not emitted (Fig. 4, $\phi = 3.77$). At last, a seventh ligament originates from the ninth stroke (Fig. 4, $\phi = 4.24$).

The ejected droplet located the farthest from the leaf tip is denoted first-in-a-burst droplet. The other droplets are named the followers. In Fig. 4, a red box is drawn around the first-in-a-burst droplet of each burst. A special focus will be made on these first droplets in the following data analysis, as they are usually ejected faster than others (cf. Sec. V B).

Influence of impact position. In Fig. 5, six impacts in the same configuration (L24, D2) with increasing impact position x_i are shown. At $x_\mathrm{i}/L = 0.35$ [Fig. 5(a)], the impacting drop spreads on the blade without reaching its edge. Consequently, no liquid sheet is formed [Fig. 5(a), $\phi = 0.25$]. The liquid residue forms a sessile drop [Fig. 5(a), $\phi = 0.75$] that slides outward on the blade in response to inertial forces [103–107], without being able to reach the leaf tip by the time the leaf oscillation is fully damped [Fig. 5(a), $\phi \geqslant 1.25$].

At $x_\mathrm{i}/L = 0.40$ [Fig. 5(b)], the spreading drop reaches the blade edge and ejections subsequent to the liquid sheet fragmentation are seen [Fig. 5(b), $\phi = 0.25$]. The angular momentum transferred to the blade is higher than at $x_\mathrm{i}/L = 0.35$. Consequently, the inertial forces are higher, and the liquid residue slides outward faster [Fig. 5(b), $0.75 \leqslant \phi \leqslant 1.5$]. As it does so, it experiences increased inertial forces, that ultimately force the ejection of a droplet at the end of the fourth stroke [Fig. 5(b), $\phi = 2$].

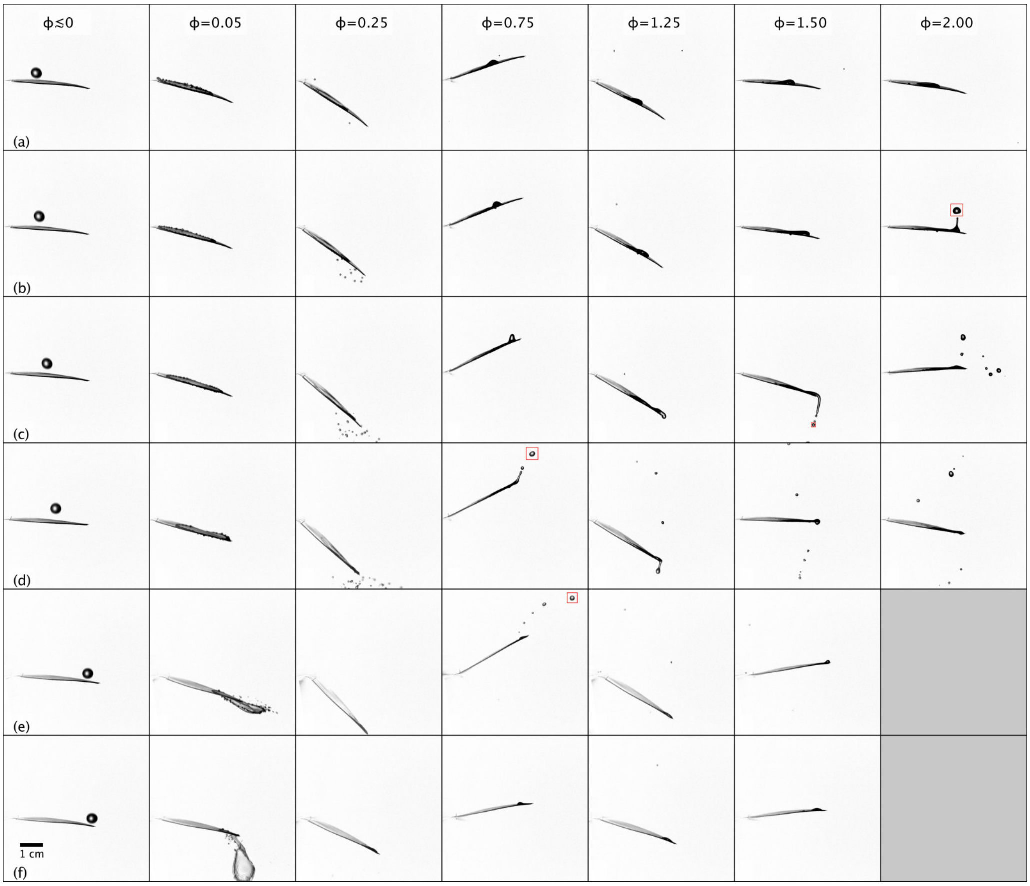

FIG. 5. Snapshots of the leaf motion and droplet ejections upon impact of drop D2 on leaf L24 (period 97 ms). Each line corresponds to a different impact point position: (a) $x_i/L = 0.35$, (b) $x_i/L = 0.4$, (c) $x_i/L = 0.5$, (d) $x_i/L = 0.6$, (e) $x_i/L = 0.85$, and (f) $x_i/L = 0.95$. Each column corresponds to a given phase ϕ. Snapshots at $\phi = 1.5$ and $\phi = 2$ for (e) and (f) are missing as the recording was stopped earlier. A red box is drawn around the first droplet of the first burst. The scale bar is 1 cm. The rotation center of the blade coincides with the left edge of each snapshot. The corresponding movies are available in the Supplemental Material [46].

As x_i/L keeps increasing, the sliding is faster, and ejections occur earlier, during the third stroke for $x_i/L = 0.50$ [Fig. 5(c)] and during both second and third strokes for $x_i/L \geqslant 0.6$ [Fig. 5(d)]. When $x_i/L = 0.85$ [Fig. 5(e)], the impact is close to the blade edge and a large volume of liquid is ejected in the initial sheet [Fig. 5(e), $\phi = 0.05$]. The remainder is ejected in a unique burst during the second stroke, as there is not enough water for two bursts [Fig. 5(e), $\phi \geqslant 0.75$]. When $x_i/L = 0.95$ [Fig. 5(f)], the drop is not entirely intercepted by the leaf blade. Consequently, the liquid sheet is not anymore in the same plane as the blade [Fig. 5(f), $\phi = 0.05$] [47]. The transfer of angular momentum is incomplete, as witnessed from the decreased inclination at $\phi = 1/4$. Inertial forces are not sufficient anymore to fragment and eject the very small liquid residue [Fig. 5(f), $\phi \geqslant 0.75$].

Influence of leaf tip angle. In Fig. 6, top views of two drop impacts on leaves are shown. Although the impact configurations are not identical, both impacts generate the same centrifugal acceleration a_c and the leaves oscillate at approximately the same frequency ω. Importantly, the leaf tip angle α differs. The first case is a drop D3 (with the highest momentum) impacting at 9.5 mm from the tip of leaf L6, with $\alpha = 45^\circ$ [Fig. 6(a)]. The drop spreads beyond the edge and forms an almost symmetrical liquid sheet [Fig. 6(a), $\phi = 0.02$] that fragments into droplets [Fig. 6(a), $\phi = 0.05$].

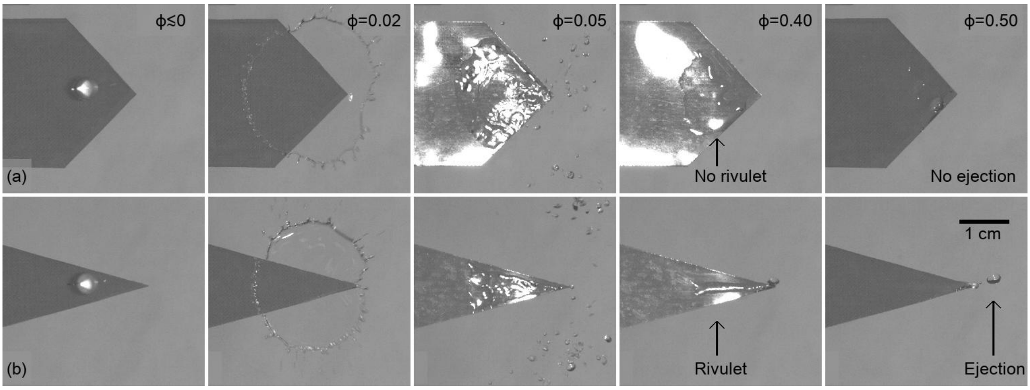

FIG. 6. Top view of two drop impacts on leaves, differing only by the leaf tip angle α: (a) Impact of a drop D3 at 9.5 mm from the tip of leaf L6 ($\alpha = 45^\circ$). (b) Impact of a drop D2 at 11.9 mm from the tip of leaf L1 ($\alpha = 15^\circ$). In both cases, the amplitude of the centrifugal acceleration right after impact is $a_c = 34.5 \pm 0.1\,\mathrm{m/s^2}$ at the leaf tip. Moreover, both leaves have approximately the same frequency $\omega \simeq 37\,\mathrm{rad/s}$ (period 170 ms). The phase ϕ at which snapshots were taken is indicated in the upper-right corner. The scale bar is 1 cm. The corresponding movie is available in the Supplemental Material [46].

At this stage, the liquid residue is still at almost its maximum spreading on the blade. It needs a significant amount of time (here a third of the leaf period) to retract, dewet, and form a thicker sessile drop in response to capillary and inertial forces [Fig. 6(a), $\phi = 0.40$]. This sessile drop is still very far from a spherical cap, which is a signature of significant contact angle hysteresis. The corresponding capillary forces here prevent the sessile drop to stretch into a ligament and eject droplets, or even to slide to the blade edge [Fig. 6(a), $\phi = 0.50$].

The second case is a drop D2, with less momentum than D3, that impacts at 11.9 mm (i.e., farther) from the leaf tip [Fig. 6(b)]. It spreads almost as far on the blade as in the first case [Fig. 6(b), $\phi = 0.02$], then the sheet fragments [Fig. 6(a), $\phi = 0.05$] and the liquid residue retracts [Fig. 6(b), $\phi = 0.40$]. Nevertheless, its initial width, in the z direction, is much smaller for $\alpha = 15^\circ$ than for $\alpha = 45^\circ$. Consequently, the retraction in z quickly leads to the formation of a longitudinal rivulet [stretched in the radial direction, Fig. 6(b), $\phi = 0.40$]. The latter is thick and its contact line along z is short, which minimizes the capillary forces resulting from contact angle hysteresis [108] and allows a strong displacement of the liquid outward in response to centrifugal forces. Ultimately, the presence of this longitudinal rivulet leads to the ejection of a droplet [Fig. 6(b), $\phi = 0.50$].

When $\alpha = 90^\circ$ (rectangle-shaped tip), for a D3 drop impacting close to the blade edge (Fig. 7), the liquid residue may be narrower in the radial direction than in the transverse (z) direction (Fig. 7, $\phi = 0.15$). Upon retraction, it forms a rivulet aligned on z, i.e., with a long contact line along z (Fig. 7, $\phi = 0.54$). The resulting hysteresis-induced capillary forces oppose a large resistance to radially outward sliding, so the rivulet does not move to the edge. Instead, it may break up in several sessile drops, in a manner reminiscent of a Rayleigh-Plateau instability (Fig. 7, $\phi = 1.57$). In the present example, the inertial forces resulting from the leaf oscillations are still sufficiently high at this step to partially eject the largest of these sessile drops (Fig. 7, $\phi = 1.96$).

Ligament breakup. As seen in Fig. 8, when a ligament is strongly stretched ($t = 75$ ms), it may almost simultaneously break up at several locations ($t = 76$ ms). Some of the fragments may recoil in single droplets (from $t = 76$ ms to $t = 78$ ms, between green and red lines), while some other fragments may further break up in smaller droplets (from $t = 78$ ms to $t = 81$ ms, below red line). In the latter case, the capillary forces that drive the ligament to recoil before it breaks up communicate a nonzero relative speed to the resulting droplets. Consequently, the droplets move toward each other, collide and almost systematically merge ($t = 88$ ms). Ultimately, the number of ejected droplets

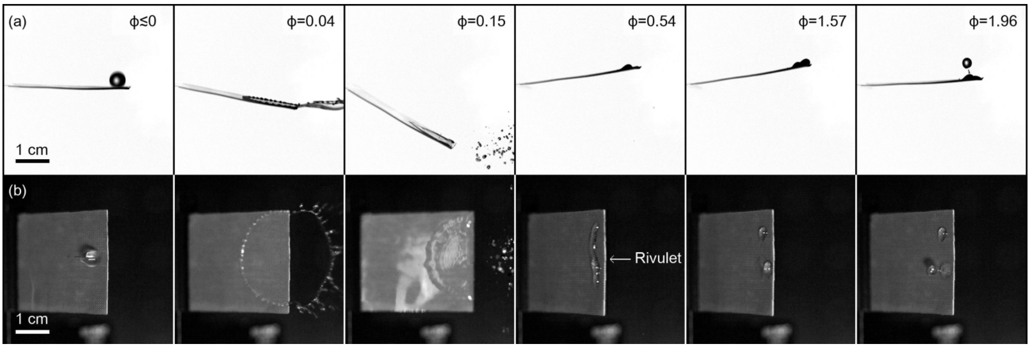

FIG. 7. Simultaneous side view (a) and top view (b) of the impact of a drop D3 at 4.0 mm from the tip of leaf L11 ($\alpha = 90^\circ$, period 98 ms). The amplitude of the centrifugal acceleration right after impact is $a_c = 45.1\ \mathrm{m/s^2}$ at the leaf tip. The phase ϕ at which snapshots were taken is indicated in the upper-right corner. The scale bar is 1 cm. The corresponding movie is available in the Supplemental Material [46].

corresponds to the initial number of ligament fragments ($t = 96$ ms). The breakup of accelerated ligaments into droplets was already investigated in a number of studies [102,109,110].

V. EXPERIMENTAL RESULTS AND DISCUSSION

A. Transfer of angular momentum at impact

At impact, the drop transfers some of its momentum to the leaf. As the leaf only rotates around the z axis ($x = 0$), we consider the transfer of angular momentum calculated from this axis. In case of a perfectly inelastic collision, the drop entirely sticks to the leaf blade after impact, and the angular momentum of the drop is entirely transferred to this "drop + leaf" system. This ideal transfer of angular momentum satisfies

$$\left(I + Mx_i^2\right)\dot{\theta}_{0t} = MVx_i, \tag{10}$$

where $M = \pi\rho D^3/6$ is the impacting drop mass and $\dot{\theta}_{0t}$ is the theoretical angular velocity of the leaf blade right after impact, assuming single-mode dynamics. In Fig. 9, the real angular velocity after impact $\dot{\theta}_0$, measured by image processing, is represented as a function of the impact point position x_i, for the configuration (L24, D2). The prediction $\dot{\theta}_{0t}$ obtained from Eq. (10) is also represented. There is a relative error of about $\pm 7\%$ on $\dot{\theta}_{0t}$ that results from uncertainties on the parameters of Eq. (10): $\pm 4\%$ for I, $\pm 2\%$ for M, much less than 1% for V, and $\pm 1\%$ for x_i. Measurements agree

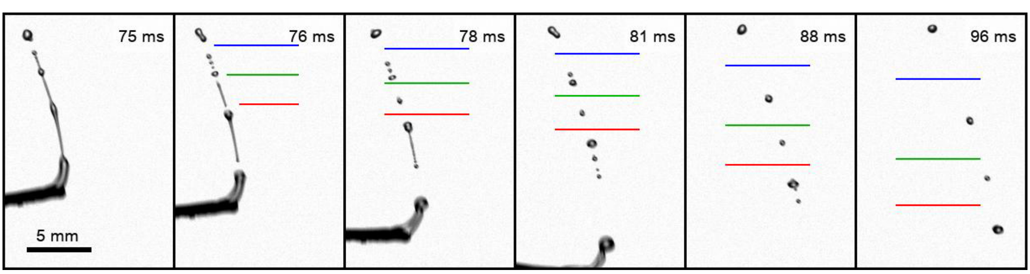

FIG. 8. Breakup and recombination of a ligament ejected from the tip of leaf L5 upon drop impact D3. Red, green and blue dashed lines are guides for the eyes that separate the ligament segments. The time after impact at which snapshots were taken is indicated in the upper-right corner. The scale bar is 5 mm. The corresponding movie is available in the Supplemental Material [46].

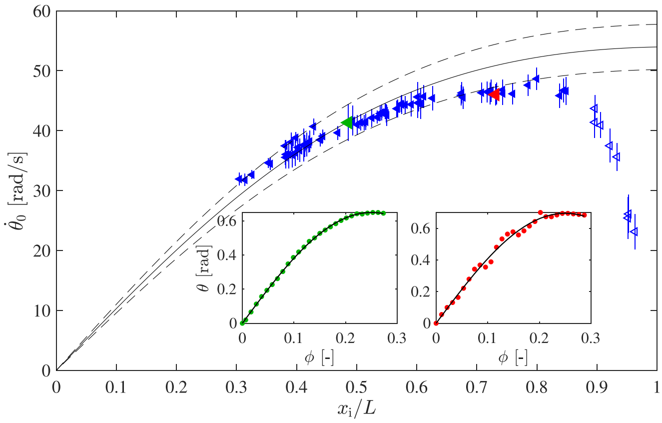

FIG. 9. Angular velocity $\dot{\theta}_0$ of the leaf blade right after impact vs impact position x_i/L (from the rotation axis in $x = 0$, normalized by leaf length). Only drop impacts of configuration (L24, D2) are represented. Symbols are emptied when the drop impacts at a distance closer than $0.85\,D$ from the leaf tip, and full otherwise. Error bars are explained in Sec. III E. The solid black line is the prediction $\dot{\theta}_{0t}$ from Eq. (10). Dashed black lines correspond to $\dot{\theta}_{0t}(\pm 7\%)$, according to uncertainties on the parameters of Eq. (10). The insets represent the time evolution of the blade inclination $\theta(\phi)$. The colored dots correspond to inclination measurements, and the black lines correspond to $\theta(\phi) = \frac{\dot{\theta}_0}{\omega}\sin(2\pi\phi)$. The angular momentum corresponding to each inset is indicated in the main plot with green and red triangles, respectively.

well with the prediction for $x_i/L < 0.6$, and become significantly smaller than the prediction for $x_i/L > 0.6$. We identify three factors that may impede this angular momentum transfer.

First, the impact point may be too close to the blade edge. Consequently, a fraction of the falling drop is not stopped by the blade and does not participate to the angular momentum transfer [Fig. 5(f)]. Concomitantly, the liquid sheet is not anymore in the plane of the blade [47]. In Fig. 9, $\dot{\theta}_0$ sharply drops when the impact point becomes closer than $0.85\,D$ from the leaf tip (empty symbols). A similar, though more extreme, decrease of momentum transfer was reported in experiments of drop impacts on fibers [86,92].

Surprisingly, for experiments in the range $x_i/L \in [0.6, 0.8]$, the measured $\dot{\theta}_0$ is still up to 15% lower than the prediction $\dot{\theta}_{0t}$ of Eq. (10) while the drop impacts sufficiently far from the blade edges to be fully deflected from its vertical fall by the blade. The second reason for a diminished transfer of momentum is revealed by a closer look at the time evolution of the blade inclination $\theta(t)$ for impacts at two different positions (insets of Fig. 9). When $x_i/L \simeq 0.49$ (green symbols in Fig. 9), the blade inclination closely follows the law $\theta = (\dot{\theta}_0/\omega)\sin(\omega t)$ during the first quarter of period of the vibration. By contrast, when $x_i/L \simeq 0.73$ (red symbols in Fig. 9), a secondary oscillation of frequency much higher than ω is superposed to the main sine function. This oscillation corresponds to a second mode of vibration of the blade, in which it rotates around an axis $x \sim 0.5$, close to its center of mass, instead of rotating around the petiole (as already mentioned in Sec. III B). This second mode is only excited when the impact point is sufficiently far from its axis of rotation, here for either $x_i/L \gtrsim 0.6$ or $x_i/L \lesssim 0.4$. The excitation of this second mode most likely explains the discrepancy between $\dot{\theta}_0$ and $\dot{\theta}_{0t}$ in the range $x_i/L \in [0.6, 0.8]$.

The third identified cause of incomplete transfer of angular momentum originates from the noninstantness of the impact [50]. The impact time is defined as D/V, namely, the characteristic time required by the drop to crush on a fixed solid surface. We define a normalized time $\tau = 2Vt/D$ and a normalized leaf frequency $\Omega = \omega D/(2V)$. The latter represents the ratio between the impact time and $1/\pi$ period of leaf oscillation. In Fig. 10, the ratio $\dot{\theta}_0/\dot{\theta}_{0t}$ is represented as a function of Ω for all the leaves. The momentum transfer is incomplete when Ω becomes of order unity, namely, when the leaf period becomes comparable to the impact time.

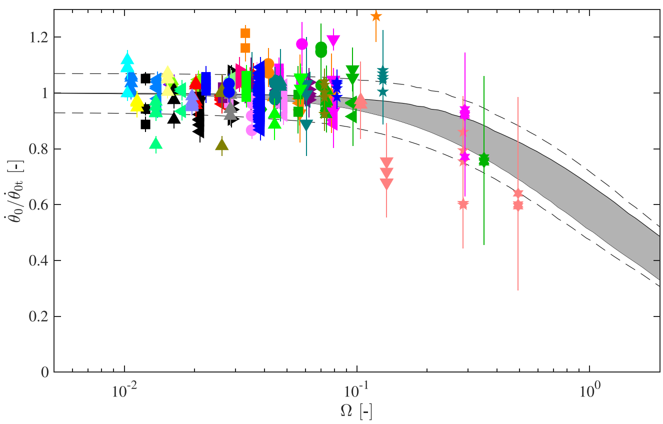

FIG. 10. Ratio between measured initial angular speed $\dot{\theta}_0$ of the leaf blade and corresponding prediction $\dot{\theta}_{0t}$, vs normalized frequency Ω. Colors and symbols represent different leaves and drop types, according to Tables II and III. Error bars are explained in Sec. III E. The grey shade corresponds to the ratio $\dot{\theta}_{0c}/\dot{\theta}_{0t}$ calculated from Eq. (17) for $\Gamma \in [0.03, 1.3]$. The dashed lines correspond to a relative error of ±7% on the prediction $\dot{\theta}_{0t}$.

Dynamics of drop impact. This fact may be rationalized by considering the time evolution of the force applied by the drop on the leaf over time. This force was measured in Ref. [50] for a drop impacting a rigid horizontal substrate, and the data are reported in Fig. 11 (a more in-depth analysis of this force can be found in Ref. [111]). The force was observed to steeply increase up to almost $F_0 = 3MV^2/(2D)$ in a time $\tau \simeq 1/4$, and decrease exponentially at later times. We approximate the force by

$$F(\tau) = F_0 e^{-\frac{3\tau}{4}}, \text{ or equivalently } F(t) = F_0 e^{-\frac{3Vt}{2D}}. \tag{11}$$

This force is normalized in such a way that

$$\int_0^\infty F\,\mathrm{d}t = MV,$$

which ensures that the drop looses all its vertical momentum upon impact. Consequently, the approximation of Eq. (11) strongly overestimates the measured force during the first instants of

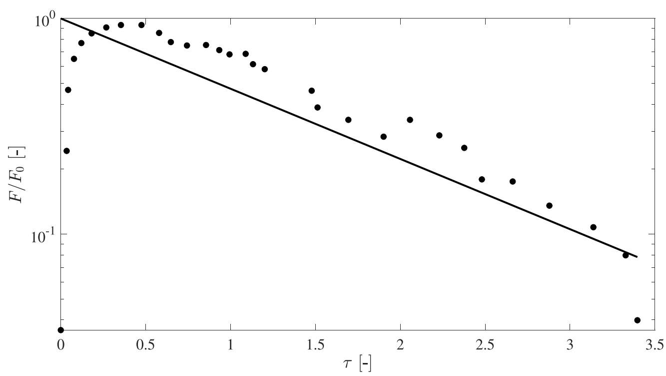

FIG. 11. Force F (normalized by F_0) exerted by a drop of diameter $D = 2.6$ mm impacting a rigid horizontal substrate at speed $V = 3$ m/s, as a function of normalized time τ. Symbols are experimental data reported in Ref. [50]. The solid line corresponds to $F = F_0 e^{-3\tau/4}$.

the impact, while it slightly underestimates the latter during the subsequent exponential decrease. From Newton's laws, the vertical position y of the center of mass of the drop must obey $M\ddot{y} = F(t)$. Substituting the approximation (11) in this equation, integrating over time, and substituting $F(t)$ back yields $F(t) \simeq -F_0\dot{y}/V$. This expression of F as a function of $\dot{y}$ is a consequence of the approximation of F by an exponential.

When a drop impacts an artificial leaf at a distance x_{i} from the center of rotation, the Newton's laws for the leaf and the drop yield (leaf damping is here neglected),

$$\begin{aligned} I\ddot{\theta} &= Fx_{\mathrm{i}} - k\theta, \\ M\ddot{y} &= F, \end{aligned} \tag{12}$$

where the velocity involved in F should now be replaced by the relative velocity between the center of mass of the drop and the leaf below the drop, namely,

$$F(t) \simeq -F_0\frac{\dot{y} + x_{\mathrm{i}}\dot{\theta}}{V}. \tag{13}$$

The initial conditions of these differential equations are $\theta(0) = 0$, $\dot{\theta}(0) = 0$, $y(0) = D/2$ and $\dot{y}(0) = -V$. We define the dimensionless variables $\tilde{y} = 2y/D$ and $\varphi = 2x_{\mathrm{i}}\theta/D$, as well as the dimensionless group

$$\Gamma = \frac{Mx_{\mathrm{i}}^2}{I}. \tag{14}$$

With these variables, Eq. (10) reads

$$\left.\frac{\mathrm{d}\varphi}{\mathrm{d}\tau}\right]_{(\tau=0)} = \frac{\Gamma}{1+\Gamma}. \tag{15}$$

The Newton's laws become

$$\frac{\mathrm{d}^2\varphi}{\mathrm{d}\tau^2} + \Omega^2\varphi = \Gamma\frac{\mathrm{d}^2\tilde{y}}{\mathrm{d}\tau^2} = -\frac{3}{4}\Gamma\frac{\mathrm{d}(\tilde{y}+\varphi)}{\mathrm{d}\tau}, \tag{16}$$

with initial conditions $\varphi = 0$, $\mathrm{d}\varphi/\mathrm{d}\tau = 0$, $\tilde{y} = 1$, and $\mathrm{d}\tilde{y}/\mathrm{d}\tau = -1$ in $\tau = 0$. These equations can be solved numerically and the corrected angular velocity can be estimated as

$$\dot{\theta}_{0\mathrm{c}} = \frac{V}{x_{\mathrm{i}}}\max_{\tau \geqslant 0}\left|\frac{\mathrm{d}\varphi}{\mathrm{d}\tau}\right|. \tag{17}$$

The ratio $\dot{\theta}_{0\mathrm{c}}/\dot{\theta}_{0\mathrm{t}}$ is reported in Fig. 10, for various Ω and for Γ in a range [0.03, 1.3] corresponding to the present experiments. This ratio indicates how much angular momentum is not transferred to the leaf owing to the noninstantness of the impact. The differential equations (16) correctly reproduce this partial transfer of angular momentum when Ω approaches 1, although the measured transfer is even lower than the prediction. The discrepancy may come from the approximation that was made on $F(t)$ in Eq. (11).

B. Droplet ejection induced by leaf motion

Droplets ejected through leaf oscillations are divided into three categories, depending on their position relative to the leaf blade at the time of their ejection: (1) vertically below the leaf blade, (2) horizontally farther than the leaf tip, and (3) vertically above the leaf blade. Droplets in the first category are typically emitted when the leaf has just passed its most downward inclination (Fig. 12), i.e., when the downward-pointing Euler force induced by the angular deceleration of the leaf is maximum. These droplets found below the blade are called downward Euler droplets. Droplets in the second category are referred as centrifugal droplets, since the centrifugal force is certainly responsible for most of their migration away from the leaf in the horizontal direction (Fig. 13). They are mostly ejected when the leaf is close to horizontal, i.e., when the centrifugal acceleration

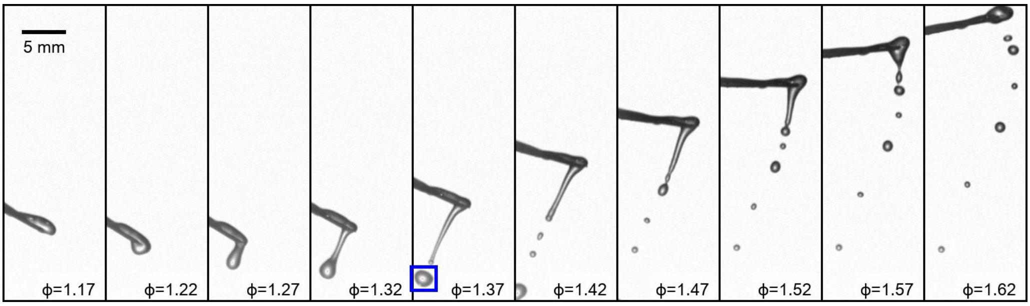

FIG. 12. Downward Euler droplet ejection, observed upon impact of a drop D2 at 15 mm from the tip of leaf L24 (period 102 ms). The phase ϕ at which snapshots were taken is reported at the bottom. The scale bar is 5 mm. The first droplet in this burst is framed in blue at the time it is ejected. The corresponding movie is available in the Supplemental Material [46].

is maximal. They correspond to the "sliding" mode described in Ref. [89]. Droplets in the third category are typically ejected shortly after the leaf reaches its highest upward inclination (Fig. 14), namely, when the upward-pointing Euler force is maximum. These droplets that are always present vertically above the blade are then named upward Euler droplets. They correspond to the pinch-off mode described in Ref. [89].

The vertical velocity v_y (positive upward) and diameter d of every droplet ejected through leaf oscillations (in all experiments) are reported in Fig. 15. The vertical velocity v_y is normalized by the characteristic velocity of the leaf tip $v_L = L\dot{\theta}_0$, while the droplet diameter is normalized by the diameter of the incoming drop D. Droplets are differentiated according to their ejection scenario (centrifugal, upward Euler or downward Euler), their time of ejection (during versus after the first leaf oscillation period), and their position in the burst (first droplet versus followers). Droplets that result from the coalescence (Fig. 8) of ligament fragments are pinpointed since their diameter is altered by this event. Similarly, droplets that bounce on each other are also pinpointed since their velocity is altered by this event. A significant segregation of droplet categories is observed in the (v_y, d) diagram: First-in-a-burst droplets are larger than followers, and the vertical velocity is higher for centrifugal droplets than for either type of Euler droplets. The normalized diameter d/D of first-in-a-burst droplets is approximately comprised between 0.2 and 0.8. This range is significantly wider than the range [0.7, 0.8] observed for such droplets formed under constant acceleration [102]. Centrifugal droplets ejected during the first period inherit from the largest upward velocity. Droplets resulting from coalescence or bouncing are not especially larger of faster than other droplets.

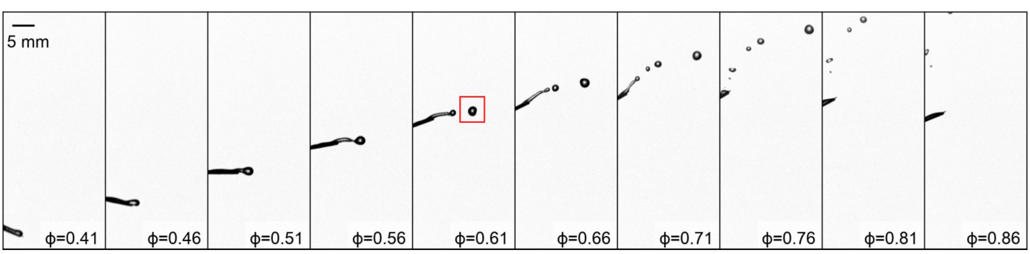

FIG. 13. Centrifugal droplet ejection, observed upon impact of a drop D2 at 7.3 mm from the tip of leaf L24 (period 102 ms). The phase ϕ at which snapshots were taken is reported at the bottom. The scale bar is 5 mm. The first droplet in this burst is framed in red at the time it is ejected. The corresponding movie is available in the Supplemental Material [46].

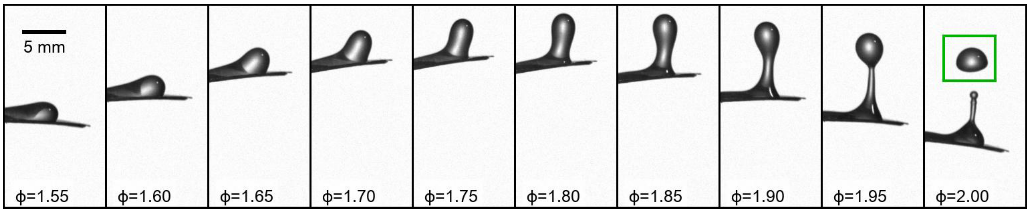

FIG. 14. Upward Euler droplet ejection, observed upon impact of a drop D2 at 22 mm from the tip of leaf L24 (period 102 ms). The phase ϕ at which snapshots were taken is reported at the bottom. The scale bar is 5 mm. The first droplet in this burst is framed in green at the time it is ejected. The corresponding movie is available in the Supplemental Material [46].

In Fig. 16, the vertical velocity v_y of ejected droplets is represented as a function of the phase ϕ_e at which they are ejected. Clearly, v_y is inherited from the velocity of the leaf tip, given by Eq. (7), with a slight delay corresponding to a phase shift $\Delta\phi_e$ of the order of $1/8$. The succession of droplet types also reflects the leaf motion: downward Euler droplets are ejected in $\phi_e \mod 1 \gtrsim 0.25$, i.e., when the leaf has just switched direction from downward to upward. Similarly, upward Euler droplets are ejected in $\phi_e \mod 1 \gtrsim 0.75$, i.e., when the leaf has just switched direction from upward to downward. Centrifugal ejections are in between, for $\phi_e \mod 0.5 < 0.25$, just after the vertical velocity of the leaf tip reached its extremum, thereby explaining why centrifugal droplets inherit the largest vertical velocity.

The horizontal velocity v_x (positive outward) of ejected droplets is represented against their vertical velocity v_y in Fig. 17, for first-in-a-burst droplets only. The accessible range of horizontal velocity is much smaller (from about -0.2 to 0.4 times v_L) than the range of vertical velocity (from about -0.9 to 0.9 times v_L), and it is equally explored by all three types of ejections. There is a positive correlation between v_x and v_y for downward Euler droplets, and a negative correlation between v_x and v_y for upward Euler droplets. By contrast, v_x does not appear to be correlated to v_y

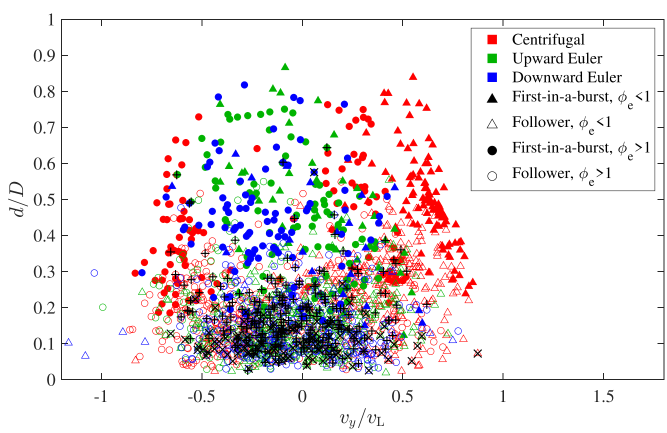

FIG. 15. Diameter d of ejected droplets (normalized by impacting drop diameter D) vs vertical velocity v_y of these droplets at the time of their ejection (normalized by leaf velocity amplitude v_L). Red, green, and blue symbols correspond to centrifugal, upward Euler and downward Euler droplets, respectively. Droplets from all the impact configurations are pooled. Full symbols represent first-in-a-burst droplets, while empty symbols represent follower droplets (i.e., any from the second in a burst). Triangles and circles correspond to droplets ejected at $\phi_e < 1$ and $\phi_e > 1$, respectively. Symbols marked with a $+$ correspond to droplets formed from the coalescence of two ejected droplets. Symbols marked with a $\times$ correspond to droplets that rebounded before being tracked.

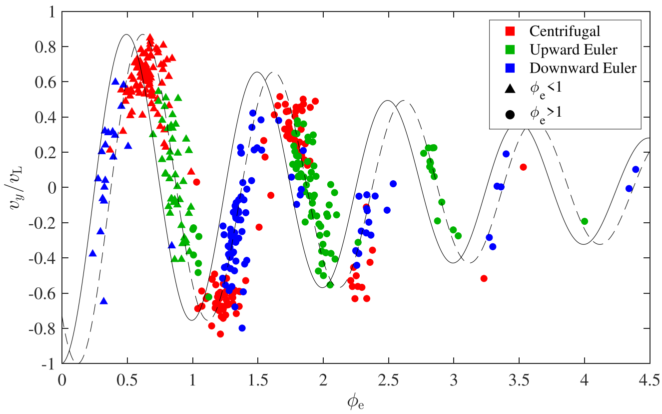

FIG. 16. Vertical velocity v_y of ejected droplets (normalized by leaf velocity amplitude v_L) as a function of the phase ϕ_e of the leaf at which they are ejected. Only first-in-a-burst droplets are represented (all impact configurations pooled). Red, green, and blue symbols correspond to centrifugal, upward Euler, and downward Euler droplets, respectively. Triangles and circles correspond to droplets ejected at $\phi_e < 1$ and $\phi_e > 1$, respectively. The solid black line represents Eq. (7), while the dotted black line represents the same function with a phase shift $\Delta\phi_e = 1/8$.

for centrifugal droplets. The speed correlation observed for Euler droplets is also likely an heritage from the leaf tip velocity: when the tip is up, its horizontal and vertical velocity components are negatively correlated, while it is the opposite when the tip is down. The larger values of v_x explored by downward Euler droplets may be the result of gravity, which naturally contributes to the sliding and downward ejection of droplets.

C. Statistics for uniformly distributed impacts

This section focuses on data from 75 drop impacts that were recorded in configuration (L24, D2) only. The impact position was distributed in $x_i/L \in [0.3, 1]$ (no ejection was observed for smaller x_i). In Fig. 18, the mass m of first-in-a-burst droplets (normalized by the mass M of the impacting

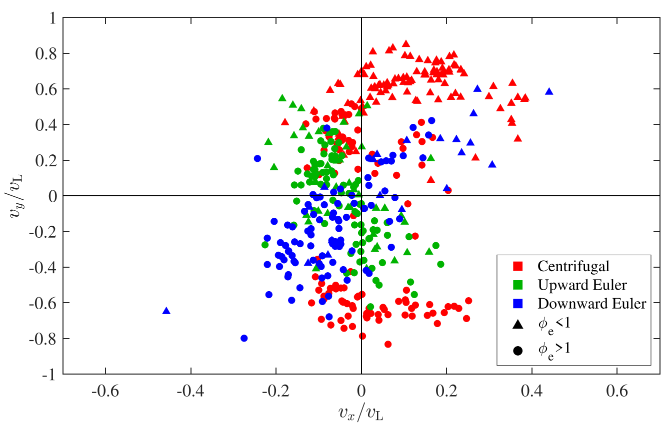

FIG. 17. Vertical velocity v_y of ejected droplets vs horizontal velocity v_x of these droplets (both normalized by leaf velocity amplitude v_L). Only first-in-a-burst droplets are represented (all impact configurations pooled). Red, green, and blue symbols correspond to centrifugal, upward Euler, and downward Euler droplets, respectively. Triangles and circles correspond to droplets ejected at $\phi_e < 1$ and $\phi_e > 1$, respectively.

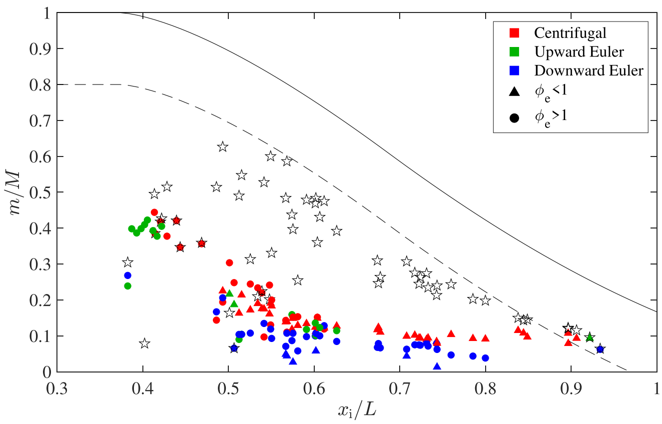

FIG. 18. Mass m of ejected droplets (normalized by impacting drop mass M) vs impact point position $x_{\rm i}$ (normalized by leaf length L). Full colored symbols correspond to the mass of first-in-a-burst droplets. Among them, red, green and blue symbols correspond to centrifugal, upward Euler, and downward Euler droplets, respectively. Triangles and circles correspond to droplets ejected at $\phi_{\rm e} < 1$ and $\phi_{\rm e} > 1$, respectively. Empty stars correspond to the total mass $m_{\rm t}$ of all droplets ejected through leaf motion in each impact. The solid black line represents $\kappa(x_{\rm i}/R_{\rm s})$, given by Eq. (B2). The dashed black line is $\kappa - 0.2$.

drop) is reported as a function of the impact position. Droplets ejected through different mechanisms are distinguished. Droplets are ejected during the first oscillation period of the leaf only when $x_{\rm i}/L > 0.5$.

The total mass $m_{\rm t}$ of droplets ejected through leaf motion is also plotted in Fig. 18. At least in the considered configuration (L24, D2), first-in-a-burst centrifugal droplets represent the largest contribution to this total ejected mass (more than one third). Although when considering individual experiments, $m_{\rm t}$ seems poorly correlated to $x_{\rm i}$ for $x_{\rm i}/L < 0.6$, its envelope for many experiments clearly decreases as the impact point approaches the leaf tip. If the drop were impacting a horizontal substrate of infinite extension, it would form a disk of radius $R_{\rm s}$ at the time of maximum spreading. We may assume that, in first approximation, the mass proportion of liquid remaining on the leaf when the sheet breaks up shortly after impact corresponds to the proportion of overlap between the disk of radius $R_{\rm s}$ and the leaf blade. This proportion κ is geometrically given by Eq. (B2), and it is plotted in Fig. 18. For $x_{\rm i}/L \in [0.5, 1]$, the envelope of $m_{\rm t}$ approximately corresponds to $\kappa - 0.2$ (dashed line in Fig. 18). In other words, at least 20% of the drop mass remaining on the leaf once the liquid sheet breaks up is never subsequently ejected through leaf motion.

We calculated the proportion $p_{\rm e}(x_{\rm i}, v_x, v_y)$ of drop mass M that is ejected as droplets with a horizontal velocity in $[v_x, v_x + {\rm d}v_x]$ and a vertical velocity in $[v_y, v_y + {\rm d}v_y]$ upon impact of that drop at position in $[x_{\rm i}, x_{\rm i} + {\rm d}x_{\rm i}]$ with speed V. In experimental data, x_i was not exactly uniformly distributed, contrary to raindrops. In the present data analysis, each measured $p_{\rm e}$ was weighed by the probability that the corresponding impact would occur at a distance $x_{\rm i}$ from the rotation axis. We define C_x as the proportion of drop mass that is ejected with a horizontal velocity $v_x > v^*$, and C_y as the proportion of drop mass that is ejected with a vertical velocity $v_y > v^*$. These variables C_x and C_y correspond to complementary cumulative distribution functions of velocities v_x and v_y, they are calculated as

$$C_x(v^*) = \frac{1}{L}\int_0^L {\rm d}x_{\rm i}\int_{-\infty}^{\infty}{\rm d}v_y\int_{v^*}^{\infty} p_{\rm e}{\rm d}v_x, \quad C_y(v^*) = \frac{1}{L}\int_0^L {\rm d}x_{\rm i}\int_{-\infty}^{\infty}{\rm d}v_x\int_{v^*}^{\infty} p_{\rm e}{\rm d}v_y, \tag{18}$$

and they are represented in Fig. 19. The distribution of v_x is close to a normal law of average $0.03V$ and standard deviation $0.036V$. The distribution of v_y is also close to a normal law, but with an average of $0.06V$ and a standard deviation of $0.118V$. The distribution of v_y is therefore significantly

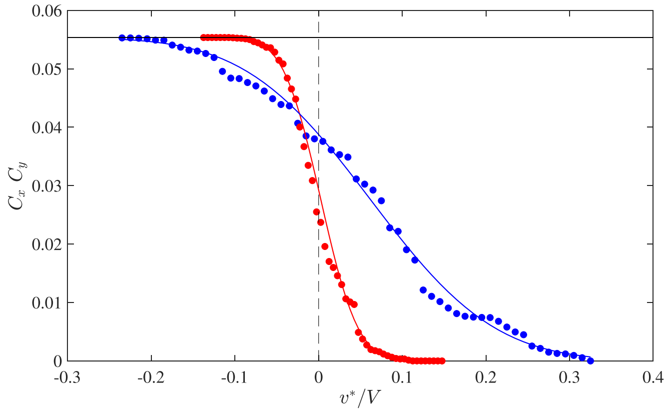

FIG. 19. Complementary cumulative distribution function C_x (proportion of impacting drop mass that is ejected with velocity $v_x > v^*$), and C_y (proportion of impacting drop mass that is ejected with velocity $v_y > v^*$), as a function of v^*/V. The red symbols correspond to calculations of C_x, while the blue symbols correspond to calculations of C_y, both from experimental data. The red and blue solid lines correspond to complementary error functions (normal distribution) fitted on these experimental data. The black solid line indicates the average proportion of drop mass that gets ejected. The dashed line corresponds to zero velocity.

more spread than the distribution of v_x. It is also significantly shifted towards positive v_y (upward ejection) while the distribution of v_x is approximately centered in $v_x = 0$. The total ejected mass is, on average, 5.5% of the impacting drop mass M (left horizontal asymptote in Fig. 19). About 0.5% of M is ejected at $v_y/V > 0.22$. Since for the considered drop D2, $V = 4.1\,\mathrm{m/s}$, $v_y \simeq 0.9\,\mathrm{m/s}$, which corresponds to an upward jump $v_y^2/(2g) > 41\,\mathrm{mm}$. In short, Fig. 19 proves that, for the considered configuration (L24,D2), droplets are ejected with a significant bias in the upward direction. In addition, it reveals that, while the amount of ejections strongly varies with impact point, on average (over a uniform distribution of impact points) there is a nonnegligible proportion of the incoming rainfall that is ejected upward.

D. Upward ejection threshold

The occurrence of upward droplet ejections results from a favorable competition of different forces: leaf-induced inertial and gravitational forces are likely to favor ejections, while liquid inertia, capillary and viscous forces are expected to inhibit ejections. Nevertheless, these forces significantly vary over the time required to eject droplets, and estimating them accurately is a challenge that revealed to be well beyond the scope of this work. The forces are also shaped by leaf properties in a nontrivial way (e.g., the unexpected dependence of ejections to the tip angle α evidenced in Figs. 6 and 7). The experiments conducted here involve not less than 12 dimensional parameters (the leaf length L, the tip angle α, the leaf frequency ω, the leaf inertia I, the drop diameter D, the drop velocity V, the impact position x_i, and the physical properties of water, including its contact angles with the leaf θ_a and θ_r, its density ρ, its surface tension σ, and its kinematic viscosity ν), reduced to nine independent dimensionless numbers according to the Buckingham π-theorem. While there must be a function of these numbers which values determine the occurrence of upward ejections, a simple expression of this presumably nonlinear function could not be found from a blind attempt. An alternative approach was taken by Erfanul Alam *et al.* [112], who successfully trained an ensemble learning algorithm to predict the occurrence of droplet ejections from a hydrophobic cantilever beam. In this work, we rather aim at obtaining a simple, closed-form function of leaf and raindrop parameters that is able to predict, to the first order, if upward droplet ejections are likely or not.

Accelerations. We take a step at simplifying the problem by focusing on which impact configurations are able to eject droplets upward (at least for some impact positions) rather than considering

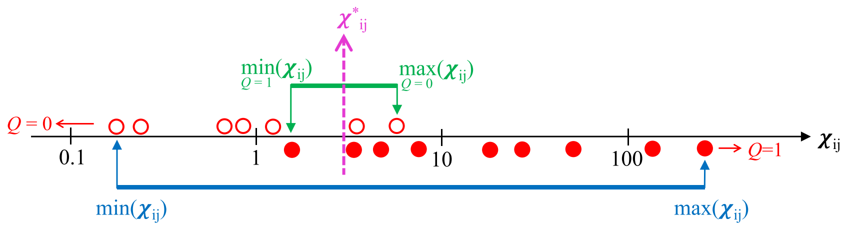

FIG. 20. Calculation of the upward ejection threshold based on the acceleration ratio χ_{ij}. The χ_{ij} axis is in logarithmic scale. Full and empty symbols correspond to subsets $Q = 1$ and $Q = 0$ of the experimental data, respectively. The length of the thick green and blue lines represent the numerator and denominator of Eq. (22), respectively. The dashed magenta arrow indicates the threshold as calculated from Eq. (23).

the full dependence of ejections to impact point. We therefore define characteristic accelerations based on the theoretical upper bound on angular speed $\dot{\theta}_{\mathrm{M}}$ achievable in each configuration,

$$\dot{\theta}_{\mathrm{M}} = \lim_{x_{\mathrm{i}}\to L} \dot{\theta}_{0\mathrm{t}} = \frac{MVL}{I + ML^2}. \tag{19}$$

The corresponding maxima of centrifugal, Euler and gravity accelerations are therefore

$$a_{\mathrm{cM}} = L\dot{\theta}_M^2, \quad a_{\mathrm{EM}} = L\dot{\theta}_{\mathrm{M}}\omega, \quad a_{\mathrm{gM}} = \frac{g\dot{\theta}_{\mathrm{M}}}{\omega}. \tag{20}$$

The gravity acceleration is here projected in the radial direction (thereby complementing the centrifugal acceleration), the projecting factor $\sin\theta$ can be approximated by $\dot{\theta}_{\mathrm{M}}/\omega$ for $\theta \ll 1$. We also define characteristic accelerations a_{i}, a_σ, and a_ν to represent the ejection-inhibiting factors, namely, the inertia of the drop, the capillary forces, and viscous dissipation, respectively:

$$a_{\mathrm{i}} = D\omega^2/2, \quad a_\sigma = \frac{4\sigma}{\rho D^2}, \quad a_\nu = \frac{2\nu\omega}{D}. \tag{21}$$

We considered an alternative definition of these three accelerations in which the impacting drop was first squeezed in a disk of diameter of the order of $D\mathrm{We}^{1/4}$ [48,113] before potentially being moved to the leaf tip and ejected. Nevertheless, we checked that such change of definition does not modify the conclusions of this section.

Prediction based on one ratio. The acceleration ratio $\chi_{ij} = a_i/a_j$ is defined as the ratio between any pair (i, j) of the six aforementioned accelerations defined in Eqs. (20) and (21). We wonder if χ_{ij} can qualify as a predictor of upward ejections ($v_y > 0$), namely, if upward ejections are possible when $\chi_{ij} > \chi^*_{ij}$ and not possible otherwise (χ^*_{ij} is then a threshold value for upward ejections). For each χ_{ij}, we associate an indicator ξ_{ij} of the prediction, defined as

$$\xi_{ij} = \frac{\max_{Q=0}(\log_{10}\chi_{ij}) - \min_{Q=1}(\log_{10}\chi_{ij})}{\max(\log_{10}\chi_{ij}) - \min(\log_{10}\chi_{ij})}, \tag{22}$$

where $Q = 1$ represents the subset of impact configurations for which some upward ejections were observed, $Q = 0$ is the complementary subset, and a function such as $\max_{Q=0}(X)$ represents the maximum of X within the subset $Q = 0$. This indicator, graphically represented in Fig. 20, quantifies how much data are correctly sorted in terms of χ_{ij}, with nonejecting configurations at small χ_{ij} and ejecting configurations at large χ_{ij}. Its numerator represents the logarithmic range over which ejecting and nonejecting configurations are mixed, while its denominator represents the full logarithmic range of χ_{ij}. A perfectly predictive ratio yields $\xi_{ij} = 0$ while a perfectly nonpredictive ratio yields $\xi_{ij} = 1$.

The values of ξ_{ij} are given in Table IV for each ratio χ_{ij}. They confirm the intuition that best-predictive ratios (i.e., smallest values of ξ_{ij}) are obtained by dividing one ejection-favoring

TABLE IV. Upward ejection indicator ξ_{ij} (in %) for each ratio of accelerations $\chi_{ij} = a_i/a_j$ (line/column). Numbers in bold correspond to values of χ_{ij} spread over more than two decades (high relevance). Numbers in brackets correspond to values of χ_{ij} spread over less than a decade (low relevance).

	a_{cM}	a_{EM}	a_{gM}	a_{i}	a_σ	a_ν
a_{cM}	–	[79%]	51%	**84%**	**24%**	62%
a_{EM}	[97%]	–	92%	86%	31%	[43%]
a_{gM}	100%	91%	–	**90%**	52%	**73%**
a_{i}	**83%**	85%	**91%**	–	**68%**	64%
a_σ	**100%**	100%	100%	**100%**	–	98%
a_ν	100%	[100%]	**100%**	100%	69%	–

acceleration (a_{cM}, a_{EM}, or a_{gM}) by one ejection-inhibiting acceleration (a_{i}, a_σ, or a_ν). Among these possibilities, the ratio a_{cM}/a_σ clearly outperforms, with nonejecting and ejecting data mixed over only 20% of the considered logarithmic range, which spreads over more than two decades. The ratio a_{EM}/a_σ also performs reasonably well. The upward ejection threshold is defined as

$$\chi_{ij}^* = \sqrt{\max_{Q=0}(\chi_{ij}) \cdot \min_{Q=1}(\chi_{ij})}. \tag{23}$$

For a_{cM}/a_σ, this threshold is $\chi^* \simeq 2.4$, while it is $\chi^* \simeq 4.1$ for a_{EM}/a_σ. Both thresholds are of order unity, which confirms that at threshold, centrifugal, Euler, and capillary accelerations are on equal terms. Both ratios a_{cM}/a_σ and a_{EM}/a_σ are therefore considered as relevant to predict the occurrence of upward ejections in first approximation. They are equivalent to Bond numbers based on centrifugal and Euler accelerations experienced by the leaf tip, respectively:

$$\mathrm{Bo_c} = \frac{a_{\mathrm{cM}}}{a_\sigma} = \frac{\rho D^2 L \dot{\theta}_{\mathrm{M}}^2}{4\sigma}, \quad \mathrm{Bo_c^*} \simeq 2.4, \quad \mathrm{Bo_E} = \frac{a_{\mathrm{EM}}}{a_\sigma} = \frac{\rho D^2 L \omega \dot{\theta}_{\mathrm{M}}}{4\sigma}, \quad \mathrm{Bo_E^*} \simeq 4.1. \tag{24}$$

A similar threshold, of $\mathrm{Bo} \simeq 2$, was determined in the simpler configuration of a sessile drop on a horizontal substrate that is vertically translated at constant acceleration [102].

Prediction based on two ratios. The occurrence of upward ejections for each impact configuration is represented in a diagram of $\mathrm{Bo_c}$ and $\mathrm{Bo_E}$ in Fig. 21. Both Bond numbers appear to be highly correlated in the present data set (correlation coefficient of 0.88 on the logarithm of these Bond numbers). The ratio $\mathrm{Bo_c}/\mathrm{Bo_E} = \dot{\theta}_{\mathrm{M}}/\omega$ corresponds to the angular amplitude of the leaf motion. Figure 21 indicates that considering $\mathrm{Bo_c}$ and $\mathrm{Bo_E}$ simultaneously does not yield a significantly better prediction of upward ejections than considering either Bond number alone.

E. Maximum droplet speed

Figure 16 suggested that the vertical velocity of ejected droplets at a given time was inherited from the leaf tip velocity an instant earlier. One might therefore expect that the maximum of upward ejection speed $\max(v_y)$ over all impacts of a given configuration corresponds to the upper bound on the leaf tip velocity v_{LM}, estimated as

$$v_{\mathrm{LM}} = L\dot{\theta}_{\mathrm{M}} = \frac{ML^2V}{I + ML^2}. \tag{25}$$

Both are represented in Fig. 22. It appears that v_{LM} is not a very good predictor of $\max(v_y)$, likely because in certain configurations, droplets are not ejected at the optimal moment (when the leaf tip has just passed its maximum upward velocity). It might also be partly due to the limited number of experiments made in each configuration (it is then unlikely that the upper bound on v_y is approached every time). Nevertheless, 70% of above-threshold configurations (for which $\mathrm{Bo_c} > \mathrm{Bo_c^*}$) ejected some droplets in the range $v_y/v_{\mathrm{LM}} \in [0.5, 1]$.

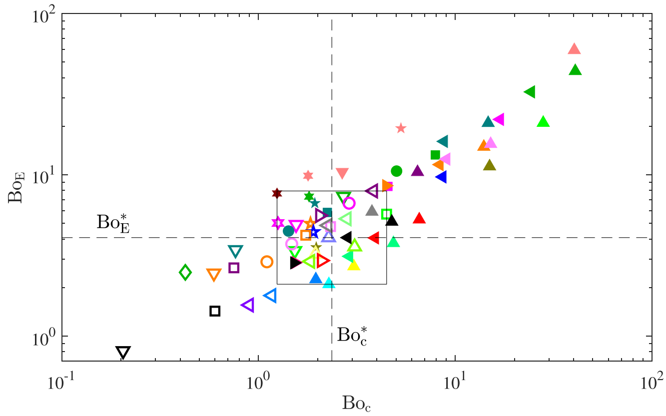

FIG. 21. Occurrence of upward ejections, in a diagram of centrifugal Bond number $\mathrm{Bo_c}$ and Euler Bond number $\mathrm{Bo_E}$ associated to each impact configuration. Colors and symbols represent different leaves and drop types, according to Tables II and III. Symbols are emptied when no upward ejections were observed, while they are full when some upward ejections were observed. The vertical and horizontal dashed lines correspond to the thresholds $\mathrm{Bo_c^*}$ and $\mathrm{Bo_E^*}$, respectively. The black box surrounds the region of the diagram in which ejecting and nonejecting configurations are mixed.

F. First-in-a-burst centrifugal droplets

In Fig. 15, it was shown that first-in-a-burst centrifugal droplets ejected during the first two leaf strokes had a larger diameter d and a larger upward velocity $v_y > 0$ than other droplets. The normalized cubed diameter $(d/D)^3$ of these droplets is represented as a function of $\mathrm{Bo_c}$ in Fig. 23. The droplet size decreases with increasing $\mathrm{Bo_c}$, in first approximation as

$$\left(\frac{d}{D}\right)^3 \simeq \mathrm{Bo_c^{-1}} \Rightarrow \rho d^3 a_{\mathrm{cM}} \sim \sigma D. \tag{26}$$

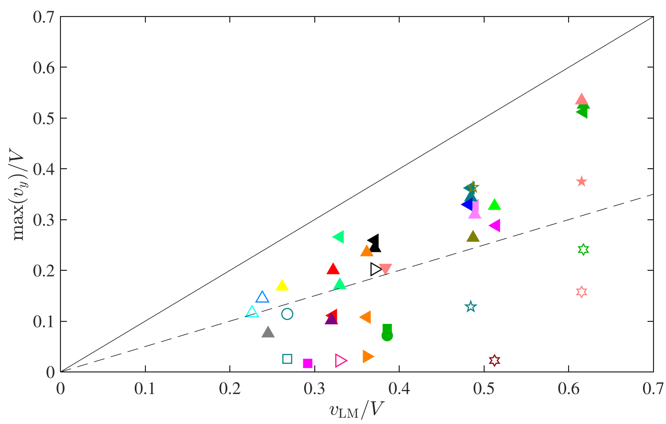

FIG. 22. Maximum upward ejection velocity v_y observed for each impact configuration as a function of the theoretical maximum leaf speed v_{LM}, both normalized by impact speed V. Colors and symbols represent different leaves and drop types, according to Tables II and III. Symbols are emptied when $\mathrm{Bo_c} < \mathrm{Bo_c^*}$, while they are full otherwise. The solid line is the parity line $\max(v_y) = v_{\mathrm{LM}}$, while the dashed line corresponds to $\max(v_y) = v_{\mathrm{LM}}/2$.

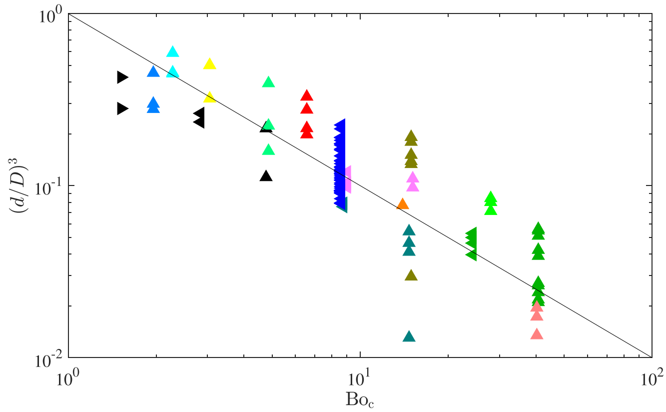

FIG. 23. Normalized cubed diameter $(d/D)^3$ of first-in-a-burst centrifugal droplets ejected during the first leaf period, as a function of the centrifugal Bond number $\mathrm{Bo_c}$. Colors and symbols represent different leaves and drop types, according to Tables II and III. Only drop types D1, D2, and D3 eject such droplets. The solid line corresponds to $(d/D)^3 = \mathrm{Bo_c^{-1}}$.

This equation is a variant of Tate's law for the detachment of pendent drops, that was already observed in other experimental investigations of droplet ejections from vibrated substrates [88,89].

VI. EXTRAPOLATION TO RAIN ON PLANT LEAVES

Previous sections have revealed that only large raindrops impacting sufficiently fast on sufficiently small leaves yield upward droplet ejections. In this section, we attempt to extrapolate these results to a realistic distribution of raindrop sizes, and to predict in which rain conditions and for which plant leaves upward ejections are significant. The goal is to provide a first-order picture with a single parameter to characterize the plant leaves and another single parameter to characterize the raindrops.

Plant leaves. We first assume that many plants with leaves of length L form a canopy without gaps. In such a configuration, every incoming raindrop is intercepted by a leaf. We attempt at expressing all other leaf parameters as functions of L. We neglect the inertia of air added mass I_a, so the inertia of the leaf I resumes to the inertia of its blade I_b, which we assume to be correlated to L. To determine this correlation, we first suppose a polynomial width profile $w(x)$ of the leaf blade:

$$w(x) = bx(L-x)(L+ax), \quad a \geqslant -1, \tag{27}$$

where $a > -1$ and $b > 0$ are constant parameters of the leaf shape. Under this assumption, the blade mass m_b and the corresponding inertia I_b can be calculated. Their ratio writes

$$\frac{I_\mathrm{b}}{m_\mathrm{b}L^2} = \frac{\int_0^L x^2 w(x)\mathrm{d}x}{L^2\int_0^L w(x)\mathrm{d}x} = \frac{2a+3}{5(a+2)}. \tag{28}$$

This rational function of a takes values in the narrow range [0.2, 0.4], so taking $I/(m_\mathrm{b}L^2) \simeq 1/3$ is a reasonable first-order approximation. According to data of the TRY database on plant leaf properties [114] (data from 321 different species reported in 46 references), the blade mass m_b is, to the first order, proportional to the leaf length squared, namely, $m_\mathrm{b}/L^2 \sim 0.06\,\mathrm{mg/mm^2}$. Therefore,

$$I \sim I_\mathrm{b} \sim CL^4, \quad C \sim 0.02\,\mathrm{mg/mm^2}. \tag{29}$$

Raindrops. In a rainfall, the speed V of raindrops is correlated to their diameter. It may be approximated by balancing their weight and the air drag that they experience during their fall:

$$c_{\mathrm{D}}\frac{\pi D^2}{4}\rho_{\mathrm{a}}\frac{V^2}{2} \simeq \frac{\pi D^3}{6}\rho g \Rightarrow V \simeq \sqrt{\frac{4\rho g D}{3c_{\mathrm{D}}\rho_{\mathrm{a}}}}, \tag{30}$$

where c_{D} is the drag coefficient, here assumed equal to 0.45 for the sake of simplicity (in reality, c_{D} is a function of the Reynolds number based on drop size and speed). A more general formulation of this relation between V and D is given in Ref. [115]. The relation is not valid for drips that originate from superjacent vegetation; their diameter is of the order of the capillary length and their velocity is mostly dictated by the height of fall.

Different types of rainfall generate different raindrop size distributions that can be approximated by functions with different parameters [116], including γ functions [117,118]. For mathematical convenience, we consider the particular case of an exponential distribution, known as a Marshall-Palmer distribution and representative of stratiform rainfalls [119]. In this distribution, the number of raindrops $N_{\mathrm{v}}\mathrm{d}D$ of diameter in the range $[D, D + \mathrm{d}D]$ per unit of air volume satisfies

$$N_{\mathrm{v}} = N_0 e^{-D/D_{\mathrm{a}}}, \quad D_{\mathrm{a}} = \frac{\int_0^\infty D N_{\mathrm{v}}\mathrm{d}D}{\int_0^\infty N_{\mathrm{v}}\mathrm{d}D}, \tag{31}$$

where D_{a} is the average raindrop diameter and $N_0 \simeq 8 \times 10^6\,\mathrm{m}^{-4}$ is a constant. This distribution tends to overestimate the number of raindrops with $D < 1$ mm, which is not an issue here since these raindrops are very unlikely to participate at all to leaf-induced ejections. The distribution also requires a cutoff for $D > D_{\mathrm{M}}$, with $D_{\mathrm{M}} \simeq 5\,\mathrm{mm}$, since larger raindrops break up as they fall [118,120]. Therefore, the exponential distribution approximates reasonably well the distribution of raindrop sizes in the range $D \in [1, 5]\,\mathrm{mm}$.

The arrival rate

$$\mathrm{d}A = V N_{\mathrm{v}}\mathrm{d}D \tag{32}$$

represents the number of raindrops of diameter $\in [D, D + \mathrm{d}D]$ that arrive at ground level, per unit of time and ground area. The rain intensity R, namely, the volume of water that reaches the ground, per unit of time and ground area, is then given by

$$R = \int_0^\infty \frac{\pi D^3}{6} V N_{\mathrm{v}}\mathrm{d}D \simeq \frac{35}{16}N_0\sqrt{\frac{\pi^3\rho g}{3\rho_{\mathrm{a}}c_{\mathrm{D}}}}D_{\mathrm{a}}^{9/2}. \tag{33}$$

From this equation, the average raindrop diameter D_{a} and the subsequent drop size distribution N_{v} associated to each rain intensity R can be found. The rain intensity is therefore the only remaining independent parameter that characterizes the rainfall.

Leaf-induced ejections. The intensity of leaf-induced ejections is here defined as the number N_{e} of raindrops, per unit of time and per unit of ground area, that are likely to generate droplet ejections reaching a certain height h_{m} above the leaf. The critical height is arbitrarily set at $h_{\mathrm{m}} = 10\,\mathrm{cm}$. Ejection would only occur if $\mathrm{Bo}_{\mathrm{c}} > \mathrm{Bo}_{\mathrm{c}}^*$. In such conditions, the expected upward velocity should satisfy $v_y \sim v_{\mathrm{LM}}/2$ (Fig. 22). Therefore, if air drag is neglected during the ascent of the droplets, then $h = \frac{v_y^2}{2g} \sim v_{\mathrm{LM}}^2/(8g)$. We define the characteristic function $\Psi(D, L)$ as equal to 1 if

$$\mathrm{Bo}_{\mathrm{c}}(D, L) = \frac{\rho/(3c_{\mathrm{D}}\rho_{\mathrm{a}})}{\left(1 + \frac{6CL^2}{\pi\rho D^3}\right)^2}\frac{\rho g D^3}{\sigma L} > \mathrm{Bo}_{\mathrm{c}}^* \quad \text{and} \quad h(D, L) = \frac{\rho/(3c_{\mathrm{D}}\rho_{\mathrm{a}})}{\left(1 + \frac{6CL^2}{\pi\rho D^3}\right)^2}\frac{D}{2} > h_m, \tag{34}$$

and 0 otherwise. Therefore, N_{e} is estimated as

$$N_{\mathrm{e}} = \int_0^\infty \Psi(D, L)\frac{\mathrm{d}A}{\mathrm{d}D}\mathrm{d}D. \tag{35}$$

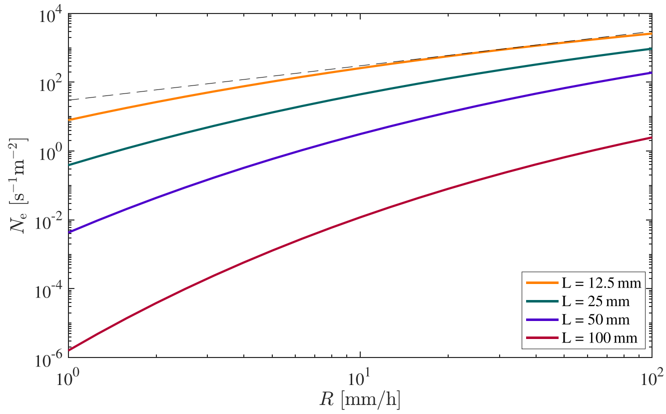

FIG. 24. Prediction of the number of raindrops N_e that eject droplets at more than 10 cm above the leaf, per unit of ground area and per unit of time, as a function of rain intensity R, for four different leaf lengths L. The dashed line represents a linear increase of N_e with R.

This prediction of N_e is calculated numerically for rain intensities in the range $R = 1$ mm/h (moderate rainfall) to $R = 100$ mm/h (extremely heavy rainfall) and for leaf lengths from $L = 12.5$ mm to 100 mm. As seen in Fig. 24, N_e increases more than proportionally with R. Consequently, a slight increase of R might greatly increase the number of upward ejection events in a given canopy. The number of ejection N_e is also extremely sensitive to leaf length L: small leaves eject considerably more droplets than large ones.

Actually, Eq. (35) overestimates the real number of raindrops that generate ejections. Indeed, as suggested in Fig. 19, only a small fraction of raindrops impact at the appropriate position for triggering ejections at velocity $v_y \sim v_{\mathrm{LM}}/2$. Nevertheless, we may expect that the qualitative dependence of N_e to both rain intensity R and leaf length L is correctly captured by Eq. (35).

The average frequency at which ejection-triggering raindrops impact a specific leaf is given by $N_e L^2$. For the considered parameters, this frequency is always less than 0.6 Hz, while most leaves able to generate ejections have natural frequencies of at least a few Hz. Therefore, most ejection-triggering impacts on a leaf will be sufficiently separated in time to be considered as independent events.

VII. CONCLUSION

Rainfalls are responsible for the dispersal of several plant pathogens between plant leaves, including in the upward direction. However, it is still unclear which mechanism at drop scale is predominantly at play to ensure this upward dispersal. The present work focused on the droplet ejections induced by the vibrations of leaves in response to raindrop impacts. We considered a simplified experimental setup in which a drop released from a dripping point impacts an artificial leaf that is initially dry. The drop spreads on the leaf and possibly beyond. Then the resulting water residue on the leaf may move and break up in response to the inertial forces from the leaf motion. Experiments were made with many different raindrops and leaves. After a qualitative description of the phenomenon, we quantified the transfer of angular momentum from the drop to the leaf and identified reasons for an incomplete transfer: impacts too close to the leaf edge, excitation of high-frequency modes of vibration of the leaf, and impact time of the same order of magnitude as the leaf period. We measured the size and speed of ejected droplets. The first droplets ejected in each burst are significantly larger than others, and they inherit the leaf speed. The distribution of the ejecta was estimated from 75 impacts of identical drops at different positions on a single leaf. In that configuration, up to 0.5% of the water mass intercepted by the leaf was ejected at more than 41 mm above that leaf. This percentage, though small, is definitely sufficient to qualify this mechanism as a possible explanation to the observed rain-induced upward dispersal of foliar diseases (e.g., Ref. [21]). Although the threshold at which droplets are ejected seems to be a complicated function of leaf and drop parameters, it corresponds, to the leading order, to a Bond number $\mathrm{Bo_c}$ (based on the centrifugal acceleration of the leaf tip) higher than 2.4. Finally, we extrapolated the results to a distribution of raindrop sizes encountered in a rainfall. The number of raindrops that induce significant upward ejection was shown to increase more than proportionally with rain intensity. Therefore, the ejection mechanism described in this work is expected to significantly increase the upward dispersal of spores in canopies at locations where climate change will induce more frequent and stronger storms.

This experimental study is based on several simplifications that need to be revisited in future work. For example, the wettability of the leaf was not varied, while plant leaves cover the entire spectrum of contact angle and contact angle hysteresis. Wettability certainly influences the spreading, recoil and sliding of the water residue at the leaf surface, and therefore modifies its potential ejection upon leaf motion. Another simplification is the consideration of individual impacts on dry leaves. In a rainfall, leaves are permanently hit by small drops that contribute to (1) a background vibration of small amplitude, and (2) the accumulation of water at the leaf surface, in the shape of sessile drops, puddles and/or thin films. This accumulated water may also be ejected through either splash or leaf oscillations, and significantly contribute to upward dispersal [25].

ACKNOWLEDGMENT

This work was supported by the Fonds de la Recherche Scientifique–FNRS through Grant No. J.0071.23.

DATA AVAILABILITY

The data supporting this study's findings are available within the article.

APPENDIX A: LEAF FREQUENCY AND DAMPING

1. Excitation with bead impacts (dry leaves)

The leaf dynamics was characterized by recording oscillations of the blade inclination $\theta(t)$ induced by the impact of a metal bead of mass 1.33 g (Fig. 25, top). The impact duration was negligible with respect to the leaf period, so it was considered as instantaneous. By contrast to drop impacts, the bead left no liquid residue on the leaf blade. The instant frequency ω and the damping ratio β/ω are reported as functions of the instant amplitude $\theta_1(t) = \theta_0 e^{-\beta t}$ in Fig. 25 (bottom).

While the frequency ω slightly increases with decreasing θ_1, the damping ratio β/ω decreases much more significantly, starting from a plateau above $\theta_1 \simeq 0.22$ rad. In first approximation, the average on all leaves yields

$$\frac{\beta}{\omega} \simeq 0.02 + 0.09\theta_1 \quad \text{if } \theta_1 < 0.22\,\text{rad}, \qquad \frac{\beta}{\omega} \simeq 0.04 \quad \text{if } \theta_1 > 0.22\,\text{rad}. \tag{A1}$$

The second term, proportional to θ_1, may be attributed to air damping. Indeed, again considering the leaf of Fig. 25 as an example, the Reynolds number is $\mathrm{Re} = L^2\omega/\nu_a \sim 5000$ (with the kinematic viscosity of the air $\nu_a \simeq 15\text{mm}^2/\text{s}$). Consequently, viscous dissipation may be neglected and the dissipated power scales as

$$P \sim 0.5\rho_a \frac{m_b}{\rho_{Ab}} L^3\dot{\theta}^3. \tag{A2}$$

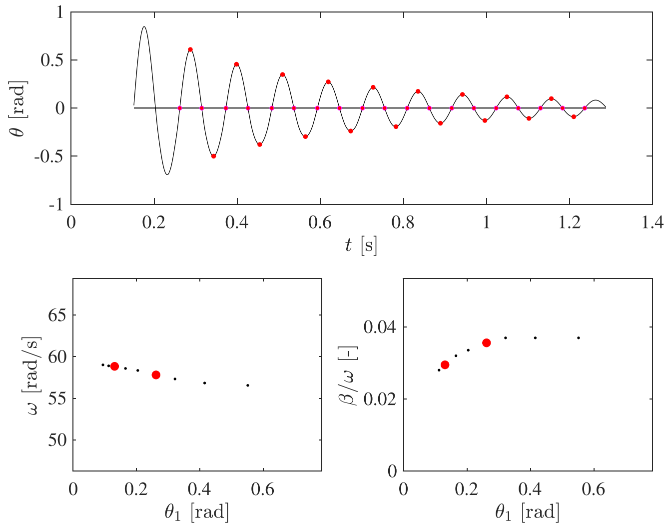

FIG. 25. Free oscillations of a leaf (L16) excited by bead impacts. (Top) Recorded blade inclination $\theta(t)$. The red dots represent the zeros and extrema of $\theta(t)$ considered to calculate both frequency and decay rate. (Bottom) Variation of the angular frequency ω (left) and the damping ratio β/ω (right) with instant oscillation amplitude $\theta_1 = \theta_0 e^{-\beta t}$. The black dots represent measurements at each period. The red dots correspond to interpolations at $\theta_1 = 0.13$ rad and $\theta_1 = 0.26$ rad.

The damping ratio is then

$$\frac{\beta}{\omega} = \frac{P}{2I_\mathrm{b}\dot{\theta}^2\omega} \sim \frac{\rho_\mathrm{a} m_\mathrm{b} L^3}{4\rho_\mathrm{Ab} I_\mathrm{b}}\theta_1 \sim 0.13\theta_1 \quad \text{for the leaf of Fig. 25.} \tag{A3}$$

The order of magnitude of this variation of β/ω with θ_1 is the same as observed experimentally. The offset $\beta/\omega \simeq 0.02$ in $\theta_1 = 0$ might be due to viscoelasticity of the petiole.

2. Excitation with drop impacts (wet leaves)

The frequency ω and damping ratio β/ω of leaf oscillations were also measured after each drop impact. The time window of this measurement started once (i) the last droplet was ejected from the leaf, and (ii) the water residue on the leaf did not slide anymore. Consequently, the inertia of the vibrating system (leaf + water residue) was assumed constant. The blade inclination still varied as $\theta(t) = \theta_0 e^{-\beta t}\sin(\omega t)$, and both ω and β/ω were measured by least-square fitting this kinematic law. In Fig. 26(a), the median of ω for all measurements in a given impact configuration is compared to the ω measured with bead impacts. Similarly, in Fig. 26(b), the median of β/ω for all measurements in a given impact configuration is compared to the β/ω measured with bead impacts.

The presence of the liquid residue induces a slight decrease of the vibration frequency. This decrease was evidenced by weighing the mass of the residue a few seconds after each impact thanks to a high-precision balance (Pioneer OHaus PX224M, accuracy 1 mg), for half of the dataset. In Fig. 27, the frequency ω measured in presence of a water residue, normalized by the extrapolation of that frequency for a residue mass $m_\mathrm{r} \to 0$, is reported as a function of the residue mass m_r, normalized by I_b/L^2. The observed frequency decrease approximately corresponds to an increase of inertia,

$$\omega \simeq \sqrt{\frac{k}{I_\mathrm{b} + m_\mathrm{r} L^2}} = \frac{\omega_{m_\mathrm{r}\to 0}}{\sqrt{1 + \frac{m_\mathrm{r} L^2}{I_\mathrm{b}}}}, \tag{A4}$$

and it is limited to 20% in the present experiments.

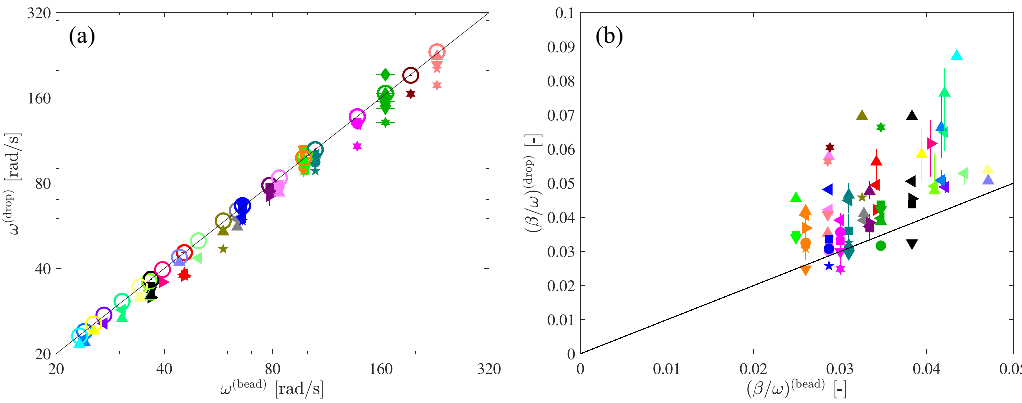

FIG. 26. Leaf frequency ω (a) and damping ratio β/ω (b), for drop impacts (subsequently wet leaves) vs bead impacts (subsequently dry leaves). Reported values of $\omega^{(\mathrm{bead})}$ correspond to the average of measured $\omega^{(\mathrm{bead})}$ at $\theta_1 = 0.13$ rad and $\theta_1 = 0.26$ rad (cf. Fig. 25). Similarly, reported values of $(\beta/\omega)^{(\mathrm{bead})}$ correspond to the average of measured $(\beta/\omega)^{(\mathrm{bead})}$ at $\theta_1 = 0.13$ rad and $\theta_1 = 0.26$ rad. The horizontal error bars represent the difference of these measurements at different θ_1. Reported values of $\omega^{(\mathrm{drop})}$ and $(\beta/\omega)^{(\mathrm{drop})}$ correspond to the median of all measurements in a given impact configuration, and associated error bars represent the interquartile range of the distributions. The black lines are bisectors corresponding to $\omega^{(\mathrm{drop})} = \omega^{(\mathrm{bead})}$ and $(\beta/\omega)^{(\mathrm{drop})} = (\beta/\omega)^{(\mathrm{bead})}$. Colors and symbols represent different leaves and drop types, according to Tables II and III.

The damping ratio may increase significantly in presence of a liquid residue, owing to the viscous dissipation of internal flows induced by the leaf vibration. This fact was already observed in Ref. [96] and rationalized in Ref. [108]. Nevertheless, β/ω remains much smaller than 1, so a significant decay of the leaf vibration is only observed after several oscillation periods. Damping ratios measured on real plant leaves excited by raindrop impacts were about $\beta/\omega \simeq 0.1$ [66], so significantly higher than in the present experiments but still of the same order of magnitude.

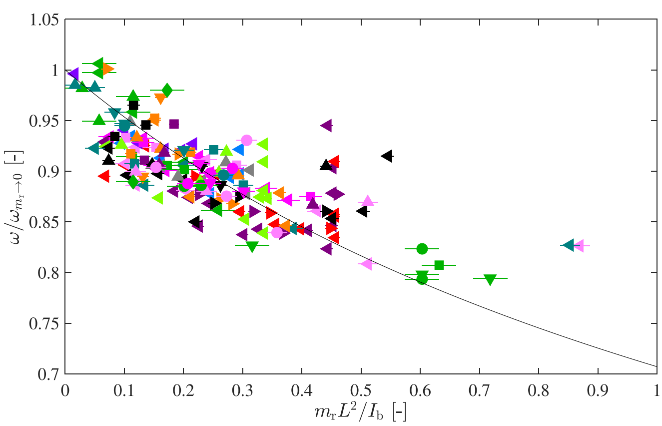

FIG. 27. Ratio between the measured leaf frequency ω in presence of a liquid residue of mass m_r and its extrapolation $\omega_{m_r\to 0}$ to a leaf with no residue, as a function of the dimensionless group $m_r L^2/I_b$. Colors and symbols represent different leaves and drop types, according to Tables II and III. The solid line corresponds to Eq. (A4).

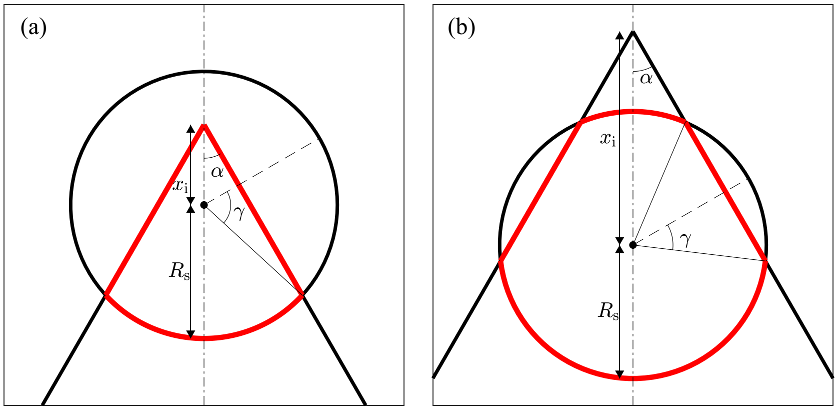

FIG. 28. Overlap area (red contour) of the leaf of tip angle α with a disk of radius R_s at a distance x_i from the leaf tip. (Left) $x_\mathrm{i}/R_\mathrm{s} < 1$, (right) $x_\mathrm{i}/R_\mathrm{s} \in [1, 1/\sin\alpha]$.

APPENDIX B: INTERSECTION OF THE LEAF BLADE WITH A DISK OF RADIUS *R* CENTERED AT A DISTANCE *d* FROM THE LEAF TIP

A drop impacting a rigid, horizontal substrate of infinite extension spreads and forms a disk that reaches a maximal diameter R_s at a certain time [101]. When a similar drop impacts a leaf blade of finite extension, the disk of radius R_s partially overlaps the blade. We aim at finding the fraction κ of the overlap area to the disk area, as a function of the distance x_i from the impact point (disk center) to the leaf tip. There are three possible cases, corresponding to $x_\mathrm{i}/R_\mathrm{s} < 1$, $x_\mathrm{i}/R_\mathrm{s} \in [1, 1/\sin\alpha]$ and $x_\mathrm{i}/R_\mathrm{s} > 1/\sin\alpha$. The first two are sketched in Fig. 28. The third case corresponds to the entire disk overlapping with the blade. We define γ as the central angle between the radius passing through the intersection point of the disk and the leaf farthest from the leaf tip, and the radius normal to the leaf edge. Elementary geometry yields

$$\cos\gamma = \frac{x_\mathrm{i}}{R_\mathrm{s}}\sin\alpha \tag{B1}$$

and

$$\kappa = \begin{cases} \frac{\frac{\pi}{2}+\alpha-\gamma+\frac{x_\mathrm{i}}{R_\mathrm{s}}\cos(\alpha-\gamma)}{\pi}, & \text{if } \frac{x_\mathrm{i}}{R_\mathrm{s}} < 1, \\ \frac{\pi-2\gamma+\sin(2\gamma)}{\pi}, & \text{if } 1 < \frac{x_\mathrm{i}}{R_\mathrm{s}} < \frac{1}{\sin\alpha}, \\ 1, & \text{if } \frac{x_\mathrm{i}}{R_\mathrm{s}} > \frac{1}{\sin\alpha}. \end{cases} \tag{B2}$$

[1] B. D. L. Fitt, H. A. McCartney, and P. J. Walklate, The role of rain in dispersal of pathogen inoculum, Annu. Rev. Phytopathol. **27**, 241 (1989).

[2] A. M. R. Almeida, R. N. R. Sibaldelli, I. O. N. Lopes, M. C. N. de Oliveira, and J. R. B. Farias, Horizontal and vertical droplet dispersion mimicking soybean—Septoria glycines pathosystem, Eur. J. Plant Pathol. **154**, 437 (2019).

[3] F. J. Bannon and B. M. Cooke, Studies on dispersal of *Septoria tritici* pycnidiospores in wheat-clover intercrops, Plant Pathol. **47**, 49 (1998).

[4] H. Mirjami Hörberg, Patterns of splash dispersed conidia of *Fusarium poae* and *Fusarium culmorum*, Eur. J. Plant Pathol. **108**, 73 (2002).

[5] V. Manstretta, E. Gourdain, and V. Rossi, Deposition patterns of *Fusarium graminearum* ascospores and conidia within a wheat canopy, Eur. J. Plant Pathol. **143**, 873 (2015).

[6] A. Pielaat, F. van den Bosch, B. D. L. Fitt, and M. J. Jeger, Simulation of vertical spread of plant diseases in a crop canopy by stem extension and splash dispersal, Ecol. Model. **151**, 195 (2002).

[7] H. Fones and S. Gurr, The impact of *Septoria tritici* blotch disease on wheat: An EU perspective, Fungal Genet. Biol. **79**, 3 (2015).

[8] T. Vidal, P. Lusley, M. Leconte, C. De Vallavieille-Pope, L. Huber, and S. Saint-Jean, Cultivar architecture modulates spore dispersal by rain splash: A new perspective to reduce disease progression in cultivar mixtures, PLoS ONE **12**, e0187788 (2017).

[9] O. J. Stedman, Patterns of unobstructed splash dispersal, Ann. Appl. Biol. **91**, 271 (1979).

[10] L. Geagea, L. Huber, I. Sache, D. Flura, H. A. McCartney, and B. D. L. Fitt, Influence of simulated rain on dispersal of rust spores from infected wheat seedlings, Agric. For. Meteorol. **101**, 53 (2000).

[11] X. Yang, L. V. Madden, D. L. Reichard, R. D. Fox, and M. A. Ellis, Motion analysis of drop impaction on a strawberry surface, Agric. For. Meteorol. **56**, 67 (1991).

[12] S. A. M. Perryman, S. J. Clark, and J. S. West, Splash dispersal of *Phyllosticta citricarpa* conidia from infected citrus fruit, Sci. Rep. **4**, 6568 (2014).

[13] P. J. Walklate, H. A. McCartney, and B. D. L. Fitt, Vertical dispersal of plant pathogens by splashing. Part II: Experimental study of the relationship between raindrop size and the maximum splash height, Plant Pathol. **38**, 64 (1989).

[14] X. Yang and L. V. Madden, Effect of ground cover, rain intensity and strawberry plants on splash of simulated raindrops, Agric. For. Meteorol. **65**, 1 (1993).

[15] P. H. Gregory, E. J. Guthrie, and M. E. Bunce, Experiments on splash dispersal of fungus spores, J. Gen. Microbiol. **20**, 328 (1959).

[16] M. W. Shaw, Variation in the height to which tracer is moved by splash during natural summer rain in the UK, Agric. For. Meteorol. **55**, 1 (1991).

[17] N. Ahimera, S. Gisler, D. P. Morgan, and T. J. Michailides, Effects of single-drop impactions and natural and simulated rains on the dispersal of *Botryosphaeria dothidea* conidia, Phytopathol. **94**, 1189 (2004).

[18] F. Fatemi and B. D. L. Fitt, Dispersal of Pseudocercosporella herpotrichoides and Pyrenopeziza brassicae spores in splash droplets, Plant Pathol. **32**, 401 (1983).

[19] J. M. Cevallos-Cevallos, M. D. Danyluk, G. Gu, G. E. Vallad, and A. H. C. van Bruggen, Dispersal of *Salmonella typhimurium* by rain splash onto tomato plants, J. Food Protect. **75**, 472 (2012).

[20] F. Suffert, I. Sache, and C. Lannou, Early stages of *Septoria tritici* blotch epidemics of winter wheat: Build-up, overseasoning, and release of primary inoculum, Plant Pathol. **60**, 166 (2011).

[21] D. J. Royle, M. W. Shaw, and R. J. Cook, Patterns of development of *Septoria nodorum* and *S. tritici* in some winter wheat crops in western europe, 1981–83, Plant Pathol. **35**, 466 (1986).

[22] D. Morais, I. Sache, F. Suffert, and V. Laval, Is the onset of *Septoria tritici* blotch epidemics related to the local pool of ascospores? Plant Pathol. **65**, 250 (2016).

[23] P. Karisto, F. Suffert, and A. Mikaberidze, Measuring splash-dispersal of a major wheat pathogen in the field, PhytoFrontiers **2**, 30 (2022).

[24] S. Saint-Jean, A. Testa, L. V. Madden, and L. Huber, Relationship between pathogen splash dispersal gradient and Weber number of impacting drops, Agric. For. Meteorol. **141**, 257 (2006).

[25] T. Gilet and L. Bourouiba, Fluid fragmentation shapes rain-induced foliar disease transmission, J. R. Soc. Interface **12**, 20141092 (2015).

[26] X. Yang, L. V. Madden, L. L. Wilson, and M. A. Ellis, Effects of surface topography and rain intensity on splash dispersal of *Colletotrichum acutatum*, Phytopathology **80**, 1115 (1990).

[27] P. J. Walklate, Vertical dispersal of plant pathogens by splashing. Part I: The theoretical relationship between rainfall and upward rain splash, Plant Pathol. **38**, 56 (1989).

[28] X. Yang, L. V. Madden, D. L. Reichard, L. L. Wilson, and M. A. Ellis, Splash dispersal of *Colletotrichum acutatum* and *Phytophthora cactorum* from strawberry fruit by single drop impactions, Phytopathology **82**, 332 (1992).

[29] B. D. L. Fitt, H. A. Mc Cartney, N. F. Creighton, M. E. Lacey, and P. J. Walklate, Dispersal of *Rhynchosporium secdis* conidia from infected barley leaves or straw by simulated rain, Ann. Appl. Biol. **112**, 49 (1988).

[30] O. C. Macdonald and H. A. McCartney, Calculation of splash droplet trajectories, Agric. For. Meteorol. **39**, 95 (1987).

[31] A. Pielaat and F. van den Bosch, A model for dispersal of plant pathogens by rainsplash, Math. Med. Biol. **15**, 117 (1998).

[32] F. Rapilly and E. Jolivet, Construction d'un modèle (episept) permettant la simulation d'une épidémie de Septoria nodorum BERK. sur blé, Rev. Stat. Appl. **24.3**, 31 (1976).

[33] C. Robert, C. Fournier, B. Andrieu, and B. Ney, Coupling a 3D virtual wheat (*Triticum aestivum*) plant model with a *Septoria tritici* epidemic model (Septo3d): A new approach to investigate plant-pathogen interactions linked to canopy architecture, Funct. Plant Biol. **35**, 997 (2008).

[34] S. Pietravalle, F. Van Den Bosch, S. J. Welham, S. R. Parker, and D. J. Lovell, Modelling of rain splash trajectories and prediction of rain splash height, Agric. For. Meteorol. **109**, 171 (2001).

[35] N. Laan, K. G. de Bruin, D. Slenter, J. Wilhelm, M. Jermy, and D. Bonn, Bloodstain pattern analysis: Implementation of a fluid dynamic model for position determination of victims, Sci. Rep. **5**, 11461 (2015).

[36] S. Saint-Jean, M. Chelle, and L. Huber, Modelling water transfer by rain-splash in a 3D canopy using Monte Carlo integration, Agric. For. Meteorol. **121**, 183 (2004).

[37] T. Vidal, C. Gigot, C. De Vallavieille-Pope, L. Huber, and S. Saint-Jean, Contrasting plant height can improve the control of rain-borne diseases in wheat cultivar mixture: Modelling splash dispersal in 3D canopies, Ann. Bot. **121**, 1299 (2018).

[38] J. Parmentier, V. Terrapon, and T. Gilet, Drop impact on thin film: Mixing, thickness variations, and ejections, Phys. Rev. Fluids **8**, 053603 (2023).

[39] Y. Wang and L. Bourouiba, Non-isolated drop impact on surfaces, J. Fluid Mech. **835**, 24 (2018).

[40] G. J. Amador, Y. Yamada, M. McCurley, and D. L. Hu, Splash-cup plants accelerate raindrops to disperse seeds, J. R. Soc. Interface **10**, 20120880 (2013).

[41] S. Kim, H. Park, H. A. Gruszewski, D. G. Schmale III, and S. Jung, Vortex-induced dispersal of a plant pathogen by raindrop impact, Proc. Natl. Acad. Sci. USA **116**, 4917 (2019).

[42] H. Park, S. Kim, H. A. Gruszewski, D. G. Schmale III, and J. Boreyko, Dynamics of splashed droplets impacting wheat leaves treated with a fungicide, J. R. Soc. Interface **17**, 20200337 (2020).

[43] B. K. van Oorschot, K. A. Bryson, O. Danner, J. E. Eklof, A. Lopez, J. Wah-Blumberg, and R. E. Pepper, Dispersal distances from splash-cup plants depend on the cup's angle and contents, J. R. Soc. Interface **21**, 20240129 (2024).

[44] S. Nath III, S. Farzad Ahmadi, H. A. Gruszewski, S. Budhiraja, C. E. Bisbano, S. Jung, D. G. Schmale III, and J. B. Boreyko, "Sneezing" plants: Pathogen transport via jumping-droplet condensation, J. R. Soc. Interface **16**, 20190243 (2019).

[45] R. Mukherjee, H. A. Gruszewski, L. T. Bilyeu, D. G. Schmale III, and J. B. Boreyko, Synergistic dispersal of plant pathogen spores by jumping-droplet condensation and wind, Proc. Natl. Acad. Sci. USA **118**, e2106938118 (2021).

[46] See Supplemental Material at http://link.aps.org/supplemental/10.1103/PhysRevFluids.10.053601 for high-speed videos and data tables.

[47] S. Lejeune, T. Gilet, and L. Bourouiba, Edge effect: Liquid sheet and droplets formed by drop impact close to an edge, Phys. Rev. Fluids **3**, 083601 (2018).

[48] S. Lejeune and T. Gilet, Drop impact close to the edge of an inclined substrate: Liquid sheet formation and breakup, Phys. Rev. Fluids **4**, 053601 (2019).

[49] T. Gilet and L. Bourouiba, Rain-induced ejection of pathogens from leaves: Revisiting the hypothesis of splash-on-film using high-speed visualization, Integr. Comp. Biol. **54**, 974 (2014).

[50] D. Soto, A. B. De Larivière, X. Boutillon, C. Clanet, and D. Quéré, The force of impacting rain, Soft Matter **10**, 4929 (2014).

[51] P. Weisensee, J. Tian, N. Miljkovic, and W. P. King, Water droplet impact on elastic superhydrophobic surfaces, Sci. Rep. **6**, 30328 (2016).

[52] T. Vasileiou, J. Gerber, J. Prautzsch, T. M. Schutzius, and D. Poulikakos, Superhydrophobicity enhancement through substrate flexibility, Proc. Natl. Acad. Sci. USA **113**, 13307 (2016).
[53] G. Upadhyay, V. Kumar, and R. Bhardwaj, Bouncing droplets on an elastic, superhydrophobic cantilever beam, Phys. Fluids **33**, 042104 (2021).
[54] C. J. Howland, A. Antkowiak, J. R. Castrejón-Pita, S. D. Howison, J. M. Oliver, R. W. Style, and A. A. Castrejón-Pita, It's harder to splash on soft solids, Phys. Rev. Lett. **117**, 184502 (2016).
[55] S. Hu, X. Cao, T. Reddyhoff, D. Puhan, S.-C. Vladescu, J. Wang, X. Shi, Z. Peng, A. J. deMello, and D. Dini, Liquid repellency enhancement through flexible microstructures, Sci. Adv. **6**, eaba9721 (2020).
[56] C. Zhang, Z. Wu, C. Shen, Y. Zheng, L. Yang, Y. Liu, and L. Ren, Effects of eigen and actual frequencies of soft elastic surfaces on droplet rebound from stationary flexible feather vanes, Soft Matter **16**, 5020 (2020).
[57] R. E. Pepper, L. Courbin, and H. A. Stone, Splashing on elastic membranes: The importance of early-time dynamics, Phys. Fluids **20**, 082103 (2008).
[58] J.-H. Kim, J. P. Rothstein, and J. K. Shang, Dynamics of a flexible superhydrophobic surface during a drop impact, Phys. Fluids **30**, 072102 (2018).
[59] P. B. Weisensee, J. Ma, Y. H. Shin, J. Tian, Y. Chang, W. P. King, and N. Miljkovic, Droplet impact on vibrating superhydrophobic surfaces, Phys. Rev. Fluids **2**, 103601 (2017).
[60] Y. Xiong, H. Huang, and X.-Y. Lu, Numerical study of droplet impact on a flexible substrate, Phys. Rev. E **101**, 053107 (2020).
[61] S. Mangili, C. Antonini, M. Marengo, and A. Amirfazli, Understanding the drop impact phenomenon on soft PDMS substrates, Soft Matter **8**, 10045 (2012).
[62] S. Chen and V. Bertola, Drop impact on spherical soft surfaces, Phys. Fluids **29**, 082106 (2017).
[63] A. Antkowiak, B. Audoly, C. Josserand, S. Neukirch, and M. Rivetti, Instant fabrication and selection of folded structures using drop impact, Proc. Natl. Acad. Sci. USA **108**, 10400 (2011).
[64] S. Gart, J. E. Mates, C. M. Megaridis, and S. Jung, Droplet impacting a cantilever: A leaf-raindrop system, Phys. Rev. Appl. **3**, 044019 (2015).
[65] Y. Bhosale, E. Esmaili, K. Bhar, and S. Jung, Bending, twisting and flapping leaf upon raindrop impact, Bioinspir. Biomim. **15**, 036007 (2020).
[66] L. K. Lauderbaugh, R. M. Ginebra-Solanellas, C. D. Holder, and R. Webb, A biomechanical model of leaf inclination angle oscillations after raindrop impact, Environ. Exp. Biol. **190**, 104586 (2021).
[67] C. D. Holder and L. K. Lauderbaugh, Progression toward maximum leaf surface storage during the rainfall interception process, Hydrol. Process. **37**, e14959 (2023).
[68] L. K. Lauderbaugh and C. D. Holder, The biomechanics of leaf oscillations during rainfall events, J. Exp. Biol. **73**, 1139 (2022).
[69] C. Der Loughian, L. Tadrist, J.-M. Allain, J. Diener, B. Moulia, and E. de Langre, Measuring local and global vibration modes in model plants, C. R. Mec. **342**, 1 (2014).
[70] E. de Langre, Plant vibrations at all scales: A review, J. Exp. Biol. **70**, 3521 (2019).
[71] S. Kim, Z. Wu, E. Esmaili, J. J. Dombroskie, and S. Jung, How a raindrop gets shattered on biological surfaces, Proc. Natl. Acad. Sci. USA **117**, 13901 (2020).
[72] A. Rozhkov, B. Prunet-Foch, and M. Vignes-Adler, Impact of water drops on small targets, Phys. Fluids **14**, 3485 (2002).
[73] A. Rozhkov, B. Prunet-Foch, and M. Vignes-Adler, Dynamics of a liquid lamella resulting from the impact of a water drop on a small target, Proc. R. Soc. London A **460**, 2681 (2004).
[74] C. Vernay, L. Ramos, and C. Ligoure, Free radially expanding liquid sheet in air: Time-and space-resolved measurement of the thickness field, J. Fluid Mech. **764**, 428 (2015).
[75] Y. Wang and L. Bourouiba, Drop impact on small surfaces: Thickness and velocity profiles of the expanding sheet in the air, J. Fluid Mech. **814**, 510 (2017).
[76] Y. Wang and L. Bourouiba, Unsteady sheet fragmentation: Droplet sizes, J. Fluid Mech. **848**, 946 (2018).
[77] Y. Wang and L. Bourouiba, Growth and breakup of ligaments in unsteady fragmentation, J. Fluid Mech. **910**, A39 (2021).
[78] Y. Wang and L. Bourouiba, Mass, momentum and energy partitioning in unsteady fragmentation, J. Fluid Mech. **935**, A29 (2022).

[79] Y. Wang and L. Bourouiba, Non-Galilean Taylor-Culick law governs sheet dynamics in unsteady fragmentation, J. Fluid Mech. **969**, A19 (2023).

[80] G. Juarez, T. Gastopoulos, Y. Zhang, M. L. Siegel, and P. E. Arratia, Splash control of drop impacts with geometric targets, Phys. Rev. E **85**, 026319 (2012).

[81] T. Bauer and T. Gilet, Rim dynamics and droplet ejections upon drop impact on star-shaped poles, Phys. Rev. Fluids **9**, 083602 (2024).

[82] H. Chen, M. Marengo, and A. Amirfazli, Drop impact onto semi-infinite solid surfaces with different wettabilities, Phys. Rev. Fluids **4**, 083601 (2019).

[83] E. Lorenceau, C. Clanet, and D. Quéré, Capturing drops with a thin fiber, J. Colloid Interface Sci. **279**, 192 (2004).

[84] S.-G. Kim and W. Kim, Drop impact on a fiber, Phys. Fluids **28**, 042001 (2016).

[85] A. P. Lebanoff and A. K. Dickerson, Drop impact onto pine needle fibers with non-circular cross section, Phys. Fluids **32**, 092113 (2020).

[86] P. Orkweha, A. Downing, A. P. Lebanoff, S. Zehtabian, S. Safa Bacanli, D. Turgut, and A. K. Dickerson, Ensemble machine learning predicts displacement of cantilevered fibers impacted by falling drops, J. Fluids Struct. **102**, 103253 (2021).

[87] M. Ryżak, M. Beczek, R. Mazur, A. Sochan, K. Gibala, C. Polakowski, and A. Bieganowski, The splash of a single water drop on selected coniferous plants, For. Ecol. Manag. **541**, 121065 (2023).

[88] A. K. Dickerson, Z. G. Mills, and D. L. Hu, Wet mammals shake at tuned frequencies to dry, J. R. Soc. Interface **9**, 3208 (2012).

[89] M. D. Erfanul Alam, J. L. Kauffman, and A. K. Dickerson, Drop ejection from vibrating damped, dampened wings, Soft Matter **16**, 1931 (2020).

[90] T. Wang, Y. Si, H. Dai, C. Li, C. Gao, Z. Dong, and L. Jiang, Apex structures enhance water drainage on leaves, Proc. Natl. Acad. Sci. USA **117**, 1890 (2020).

[91] C. D. Holder, L. K. Lauderbaugh, R. M. Ginebra-Solanellas, and R. Webb, Changes in leaf inclination angle as an indicator of progression toward leaf surface storage during the rainfall interception process, J. Hydrol. **588**, 125070 (2020).

[92] J. Comtet, B. Keshavarz, and J. W. M. Bush, Drop impact and capture on a thin flexible fiber, Soft Matter **12**, 149 (2016).

[93] B. Moulia, Leaves as shell structures: Double curvature, auto-stresses, and minimal mechanical energy constraints on leaf rolling in grasses, J. Plant Growth Regul. **19**, 19 (2000).

[94] J.-F. Louf, L. Nelson, H. Kang, P. N. Song, T. Zehnbauer, and S. Jung, How wind drives the correlation between leaf shape and mechanical properties, Sci. Rep. **8**, 16314 (2018).

[95] C. E. Brennen, A review of added mass and fluid inertial forces, Tech. Rep. No. N62583-81-MR-554 (Naval Civil Eng. Lab Port Hueneme, CA, 1982).

[96] M. D. Erfanul Alam and A. K. Dickerson, Sessile liquid drops damp vibrating structures, Phys. Fluids **33**, 062113 (2021).

[97] C. Clanet and J.-C. Lasheras, Transition from dripping to jetting, J. Fluid Mech. **383**, 307 (1999).

[98] D. F. Levia, K. Nanko, H. Amasaki, T. W. Giambelluca, N. Iida S. Hotta, R. G. Mudd, M. A. Nullet, N. Sakai, Y. Shinohara, X. Sun, C. Tantasirin, and K. Yamada, Throughfall partitioning by trees, Hydrol. Process. **33**, 1698 (2019).

[99] K. Nanko, Y. Onda, A. Ito, and H. Moriwaki, Spatial variability of throughfall under a single tree: Experimental study of rainfall amount, raindrops, and kinetic energy, Agric. For. Meteorol. **151**, 1173 (2011).

[100] J. Parmentier, S. Lejeune, M. Maréchal, F. Bourges, D. Genty, V. Terrapon, J.-C. Maréchal, and T. Gilet, A drop does not fall in a straight line: A rationale for the width of stalagmites, Proc. R. Soc. A **475**, 20190556 (2019).

[101] N. Laan, K. G. de Bruin, D. Bartolo, C. Josserand, and D. Bonn, Maximum diameter of impacting liquid droplets, Phys. Rev. Appl. **2**, 044018 (2014).

[102] N. Shen, Y. Kulkarni, T. Jamin, S. Popinet, S. Zaleski, and L. Bourouiba, Fragmentation from inertial detachment of a sessile droplet: Implications for pathogen transport, J. Fluid Mech. **1002**, A6 (2025).

[103] N. Le Grand, A. Daerr, and L. Limat, Shape and motion of drops sliding down an inclined plane, J. Fluid Mech. **541**, 293 (2005).
[104] P. Brunet, J. Eggers, and R. D. Deegan, Vibration-induced climbing of drops, Phys. Rev. Lett. **99**, 144501 (2007).
[105] X. Noblin, R. Kofman, and F. Celestini, Ratchetlike motion of a shaken drop, Phys. Rev. Lett. **102**, 194504 (2009).
[106] P. Sartori, D. Quagliati, S. Varagnolo, M. Pierno, G. Mistura, F. Magaletti, and C. M. Casciola, Drop motion induced by vertical vibrations, New J. Phys. **17**, 113017 (2015).
[107] M. Costalonga and P. Brunet, Directional motion of vibrated sessile drops: A quantitative study, Phys. Rev. Fluids **5**, 023601 (2020).
[108] T. Gilet, Cuboid drop: A low-dimensional model of drop dynamics on a substrate, Phys. Rev. Fluids **9**, 043601 (2024).
[109] P. Marmottant and E. Villermaux, Fragmentation of stretched liquid ligaments, Phys. Fluids **16**, 2732 (2004).
[110] Y. E. Kamis, S. Prakash, W.-P. Breugem, and H. B. Eral, Controlling the breakup of spiralling jets: Results from experiments, nonlinear simulations and linear stability analysis, J. Fluid Mech. **956**, A24 (2023).
[111] L. Gordillo, T.-P. Sun, and X. Cheng, Dynamics of drop impact on solid surfaces: Evolution of impact force and self-similar spreading, J. Fluid Mech. **840**, 190 (2018).
[112] M. D. Erfanul Alam, D. Wu, and A. K. Dickerson, Predictive modelling of drop ejection from damped, dampened wings by machine learning, Proc. R. Soc. A **476**, 20200467 (2021).
[113] C. Clanet, C. Beguin, D. Richard, and D. Quéré, Maximal deformation of an impacting drop, J. Fluid Mech. **517**, 199 (2004).
[114] J. Kattge *et al.*, Try plant trait database-enhanced coverage and open access, Global Change Biol. **26**, 119 (2020).
[115] R. Uijlenhoet and J. N. M. Stricker, A consistent rainfall parameterization based on the exponential raindrop size distribution, J. Hydrol. **218**, 101 (1999).
[116] E. Adirosi, E. Volpi, F. Lombardo, and L. Baldini, Raindrop size distribution: Fitting performance of common theoretical models, Adv. Water Resour. **96**, 290 (2016).
[117] C. W. Ulbrich, Natural variations in the analytical form of the raindrop size distribution, J. Appl. Meteorol. Climatol. **22**, 1764 (1983).
[118] E. Villermaux and B. Bossa, Single-drop fragmentation determines size distribution of raindrops, Nat. Phys. **5**, 697 (2009).
[119] J. S. Marshall and W. McK. Palmer, The distribution of raindrops with size, J. Meteorol. **5**, 165 (1948).
[120] É. Reyssat, F. Chevy, A.-L. Biance, L. Petitjean, and D. Quéré, Shape and instability of free-falling liquid globules, Europhys. Lett. **80**, 34005 (2007).